ATLAS NOTE

ATLAS-CONF-2017-022

22nd March 2017

Search for squarks and gluinos in final states with jets and missing transverse momentum using 36 fb^{-1} of $\sqrt{s}$ =13 TeV pp collision data with the ATLAS detector

The ATLAS Collaboration

Abstract

A search for the supersymmetric partners of quarks and gluons (squarks and gluinos) in final states containing hadronic jets and missing transverse momentum, but no electrons or muons, is presented. The data used in this search were recorded in 2015 and 2016 by the ATLAS experiment in $\sqrt{s}$ = 13 TeV proton–proton collisions at the Large Hadron Collider, corresponding to an integrated luminosity of 36.1 fb^{-1}. The results are interpreted in the context of various models where squarks and gluinos are pair-produced and the neutralino is the lightest supersymmetric particle. An exclusion limit at the 95% confidence level on the mass of the gluino is set at 2.03 TeV for a simplified model incorporating only a gluino and the lightest neutralino, assuming the lightest neutralino is massless. For a simplified model involving the strong production of mass-degenerate first- and second-generation squarks, squark masses below 1.58 TeV are excluded for a massless lightest neutralino. These limits substantially extend the region of supersymmetric parameter space excluded by previous searches with the ATLAS detector.

1 Introduction

Supersymmetry (SUSY) [1–6] is a generalization of space-time symmetries that predicts new bosonic partners for the fermions and new fermionic partners for the bosons of the Standard Model (SM). If R-parity is conserved [7], SUSY particles (called sparticles) are produced in pairs and the lightest supersymmetric particle (LSP) is stable and represents a possible dark-matter candidate. The scalar partners of the left- and right-handed quarks, the squarks $\tilde{q}_L$ and $\tilde{q}_R$, mix to form two mass eigenstates $\tilde{q}_1$ and $\tilde{q}_2$ ordered by increasing mass. Superpartners of the charged and neutral electroweak and Higgs bosons also mix to produce charginos ($\tilde{\chi}^\pm$) and neutralinos ($\tilde{\chi}^0$). Squarks and the fermionic partners of the gluons, the gluinos ($\tilde{g}$), could be produced in strong-interaction processes at the Large Hadron Collider (LHC) [8] and decay via cascades ending with the stable LSP, which escapes the detector unseen, producing substantial missing transverse momentum (E_T^{miss}).

The large expected cross-sections predicted for the strong production of supersymmetric particles make the production of gluinos and squarks a primary target in searches for SUSY in proton–proton (pp) collisions at a centre-of-mass energy of 13 TeV at the LHC. Interest in these searches is motivated by the large number of R-parity-conserving models in the Minimal Supersymmetric Standard Model (MSSM) [9, 10] in which squarks (including anti-squarks) and gluinos can be produced in pairs ($\tilde{g}\tilde{g}$, $\tilde{q}\tilde{q}$, $\tilde{q}\tilde{g}$) and can decay through $\tilde{q} \to q\tilde{\chi}_1^0$ and $\tilde{g} \to q\bar{q}\tilde{\chi}_1^0$ to the lightest neutralino, $\tilde{\chi}_1^0$, assumed to be the LSP. Additional decay modes can include the production of charginos via $\tilde{q} \to q\tilde{\chi}^\pm$ (where $\tilde{q}$ and q are of different flavour) and $\tilde{g} \to qq\tilde{\chi}^\pm$, or neutralinos via $\tilde{g} \to qq\tilde{\chi}_2^0$. Subsequent chargino decay to $W^\pm\tilde{\chi}_1^0$ or neutralino decay to $Z\tilde{\chi}_1^0$ or $h\tilde{\chi}_1^0$, depending on the decay modes of W, Z and h bosons, can increase the jet multiplicity and missing transverse momentum.

This paper presents two approaches to search for these sparticles in final states containing only hadronic jets and large missing transverse momentum. The first is an update of the analysis [11] (referred to as 'Meff-based search' in the following). The second is a complementary search using the Recursive Jigsaw Reconstruction (RJR) techniques [12, 13] in the construction of a discriminating variable set ('RJR-based search'). By using a dedicated set of selection criteria, the RJR-search improves the sensitivity to supersymmetric models with small mass splittings between the sparticles (models with compressed spectra). Both searches presented here adopt the same general approach as the analysis of the 7 TeV, 8 TeV and 13 TeV data collected during Run 1 and Run 2 of the LHC, described in Refs. [11, 14–18]. The CMS Collaboration has set limits on similar models in Refs. [19–27].

In the searches presented here, events with reconstructed electrons or muons are rejected to avoid any overlap with a complementary ATLAS search in final states with one lepton, jets and missing transverse momentum [28], and to reduce the background from events with neutrinos ($W \to e\nu, \mu\nu$). The selection criteria are optimized in the ($m_{\tilde{g}}, m_{\tilde{\chi}_1^0}$) and ($m_{\tilde{q}}, m_{\tilde{\chi}_1^0}$) planes, (where $m_{\tilde{g}}$, $m_{\tilde{q}}$ and $m_{\tilde{\chi}_1^0}$ are the gluino, squark and the LSP masses, respectively) for simplified models [29–31] in which all other supersymmetric particles have masses beyond the reach of the LHC, and in the ($m_{\tilde{g}}, m_{\tilde{q}}$) plane for the simplified phenomenological MSSM (pMSSM) models [32, 33] in which the number of MSSM parameters is reduced based on existing experimental and theoretical constraints. Although interpreted in terms of SUSY models, the results of this analysis could also constrain any model of new physics that predicts the production of jets in association with missing transverse momentum.

The paper is organized as follows. Section 2 describes the ATLAS experiment and the data sample used, and Section 3 the Monte Carlo (MC) simulation samples used for background and signal modelling. The object reconstruction and identification are presented in Section 4. The analysis strategy used by both

searches is given in Section 5. Searches are performed in signal regions which are defined in Section 7. Since the Recursive Jigsaw technique is a new approach for this search and it uses complex variables, Section 6 is dedicated to the description of the technique and associated variables. Summaries of the background estimation methodology and corresponding systematic uncertainties are presented in Sections 8 and 9, respectively. Results obtained using the signal regions optimized for both searches are reported in Section 10. Section 11 is devoted to conclusions.

2 The ATLAS detector and data samples

The ATLAS detector [34] is a multi-purpose detector with a forward-backward symmetric cylindrical geometry and nearly 4π coverage in solid angle.[1] The inner tracking detector (ID) consists of pixel and silicon microstrip detectors covering the pseudorapidity region $|\eta| < 2.5$, surrounded by a transition radiation tracker which improves electron identification over the region $|\eta| < 2.0$. The innermost pixel layer, the insertable B-layer [35], was added between Run 1 and Run 2 of the LHC, at a radius of 33 mm around a new, narrower and thinner beam pipe. The ID is surrounded by a thin superconducting solenoid providing an axial 2 T magnetic field and by a fine-granularity lead/liquid-argon (LAr) electromagnetic calorimeter covering $|\eta| < 3.2$. A steel/scintillator-tile calorimeter provides hadronic coverage in the central pseudorapidity range ($|\eta| < 1.7$). The endcap and forward regions ($1.5 < |\eta| < 4.9$) are made of LAr active layers with either copper or tungsten as the absorber material for electromagnetic and hadronic measurements. The muon spectrometer with an air-core toroid magnet system surrounds the calorimeters. Three layers of high-precision tracking chambers provide coverage in the range $|\eta| < 2.7$, while dedicated chambers allow triggering in the region $|\eta| < 2.4$.

The ATLAS trigger system [36] consists of two levels; the first level is a hardware-based system, while the second is a software-based system called the high-level Trigger. The events used by the searches were selected using a trigger logic that accepts events with a missing transverse momentum above 70 GeV (for data collected during 2015) or 90–110 GeV (depending on data taking period for data collected in 2016) calculated using a vectorial sum of the jet transverse momenta. The trigger is 100% efficient for the event selections considered in these analyses. Auxiliary data samples used to estimate the yields of background events were selected using triggers requiring at least one isolated electron ($p_T > 24$ GeV), muon ($p_T > 20$ GeV) or photon ($p_T > 120$ GeV) for data collected in 2015. For the 2016 data, the background events were selected using triggers requiring at least one isolated electron or muon ($p_T > 26$ GeV) or photon ($p_T > 140$ GeV).

The data were collected by the ATLAS detector during 2015 with a peak delivered instantaneous luminosity of $L = 5.2 \times 10^{33}$ cm^{-2}s^{-1}, and during 2016 with a corresponding peak delivered instantaneous luminosity of 1.37×10^{34} cm^{-2}s^{-1}, with a mean number of additional pp interactions per bunch crossing in the dataset of $\langle\mu\rangle = 14$ in 2015 and $\langle\mu\rangle = 24$ in 2016. Application of beam, detector and data-quality criteria resulted in a total integrated luminosity of 36.1 fb^{-1}. The uncertainty on the integrated luminosity is ±3.2%. It is derived, following a methodology similar to that detailed in Ref. [37], from a preliminary

---

[1] ATLAS uses a right-handed coordinate system with its origin at the nominal interaction point in the centre of the detector. The positive x-axis is defined by the direction from the interaction point to the centre of the LHC ring, with the positive y-axis pointing upwards, while the beam direction defines the z-axis. Cylindrical coordinates (r, ϕ) are used in the transverse plane, ϕ being the azimuthal angle around the z-axis. The pseudorapidity η is defined in terms of the polar angle θ by $\eta = -\ln\tan(\theta/2)$ and the rapidity is defined as $y = (1/2)\ln[(E + p_z)/(E - p_z)]$ where E is the energy and p_z the longitudinal momentum of the object of interest. The transverse momentum p_T, the transverse energy E_T and the missing transverse momentum E_T^{miss} are defined in the x–y plane unless stated otherwise.

calibration of the luminosity scale using a pair of x–y beam-separation scans performed in August 2015 and May 2016.

3 Monte Carlo simulated samples

A set of simulated Monte Carlo (MC) data samples is used to optimize the selections, estimate backgrounds and assess the sensitivity to specific SUSY signal models.

Both simplied models and pMSSM models are used as SUSY signals in this paper. Simplified models are defined by an effective Lagrangian describing the interactions of a small number of new particles, assuming one production process and one decay channel with a 100% branching fraction. Signal samples are used to describe squark- and gluino-pair production, followed by the direct ($\tilde{q} \rightarrow q\tilde{\chi}^0_1$) or one-step ($\tilde{q} \rightarrow qW\tilde{\chi}^0_1$) decays of squarks and direct ($\tilde{g} \rightarrow qq\tilde{\chi}^0_1$) or one-step ($\tilde{g} \rightarrow qqW\tilde{\chi}^0_1$, $\tilde{g} \rightarrow qqZ\tilde{\chi}^0_1$) decays of gluinos as shown in Figure 1. Direct decays are those where the considered SUSY particles decay directly into SM particles and the LSP, while the one-step decays refer to the cases where the decays occur via one intermediate on-shell SUSY particle, as indicated in parentheses. In pMSSM models, gluino and first and second generation squark production are considered inclusively, followed by direct decays of squarks and gluinos, or decays of squarks via gluino ($\tilde{q} \rightarrow q\tilde{g}$) and decays of gluinos via squarks ($\tilde{g} \rightarrow q\tilde{q}$) if kinematically possible. All other supersymmetric particles, including the squarks of the third generation, have their masses effectively decoupled. These samples are generated with up to two (simplified models) or one (pMSSM models) extra partons in the matrix element using MG5_aMC@NLO 2.2.2 or 2.3.3 event generator [38] interfaced to Pythia 8.186 [39]. The CKKW-L merging scheme [40] is applied with a scale parameter that is set to a quarter of the mass of the gluino for $\tilde{g}\tilde{g}$ production or of the squark for $\tilde{q}\tilde{q}$ production in simplified models. In pMSSM models, a quarter of the lower mass of the gluino or the squark is used for CKKW-L merging scale. The A14 [41] set of tuned parameters (tune) is used for ISR/FSR and underlying event (MPI) parameters together with the NNPDF2.3LO [42] parton distribution function (PDF) set. The signal cross-sections are calculated at next-to-leading order (NLO) in the strong coupling constant, adding the resummation of soft gluon emission at next-to-leading-logarithmic accuracy (NLO+NLL) [43–47]. The nominal squark and gluino cross-sections are taken from an envelope of predictions using different PDF sets and factorization and renormalization scales, as described in Ref. [48], considering only light-flavour squarks ($\tilde{u}$, $\tilde{d}$, $\tilde{s}$, $\tilde{c}$). Eight times degeneracy of squarks is assumed for the simplified models with direct decays of squarks and pMSSM models while four times degeneracy is assumed for the simplified models with one-step decays of squarks. For the light-flavour squarks (gluinos) in case of gluino-pair (squark-pair) production in simplified models, cross-sections are evaluated assuming masses of 450 TeV. The free parameters are $m_{\tilde{\chi}^0_1}$ and $m_{\tilde{q}}$ ($m_{\tilde{g}}$) for gluino-pair (squark-pair) production models in simplified models, while $m_{\tilde{q}}$ and $m_{\tilde{g}}$ are varied in pMSSM models while fixing $m_{\tilde{\chi}^0_1}$.

The production of W or Z/γ^* bosons in association with jets [49] is simulated using the Sherpa 2.2.1 generator [50], while the production of γ in association with jets is simulated using the Sherpa 2.1.1 generator. For W or Z bosons, the matrix elements are calculated for up to two partons at NLO and up to two additional partons at leading order (LO) using the Commies [51] and Olenolin's [52] matrix-element generators, and merged with the Sherpa parton shower [53] using the ME+PS@NLO prescription [54]. Events containing a photon in association with jets are generated requiring a photon transverse momentum above 35 GeV. For these events, matrix elements are calculated at LO with up to three or four partons depending on the p_T of the photon, and merged with the Sherpa parton shower using the ME+PS@LO
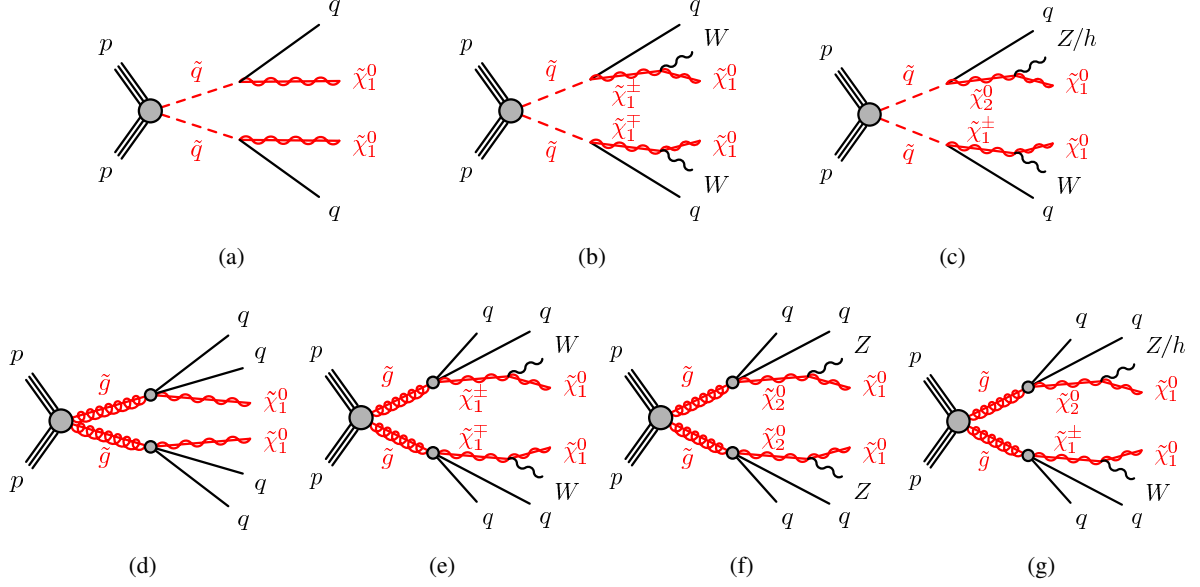
Figure 1: The decay topologies of (a,b,c) squark-pair production and (d, e, f, g) gluino-pair production in the simplified models with (a) direct or (b,c) one-step decays of squarks and (d) direct or (e, f, g) one-step decays of gluinos.

prescription [55]. In the case of W/Z+jets, the NNPDF3.0NNLO PDF set [56] is used, while for the γ+jets production the CT10 PDF set [57] is used, both in conjunction with dedicated parton shower-tuning developed by the authors of SHERPA. The W/Z + jets events are normalized to their NNLO cross-sections [58]. For the γ+jets process the LO cross-section, taken directly from the SHERPA MC generator, is multiplied by a correction factor as described in Section 8.

For the generation of $t\bar{t}$ and single-top processes in the Wt and s-channel [59], the POWHEG-BOX v2 [60] generator is used with the CT10 PDF set. The electroweak (EV) t-channel single-top events are modelled using the POWHEG-BOX v1 generator. This generator uses the four-flavour scheme for the NLO matrix-element calculations together with the fixed four-flavour PDF set CT10f4 [57]. For these processes, the decay of the top quark is simulated using MADSPIN [61] preserving all spin correlations, while for all processes the parton shower, fragmentation, and the underlying event are generated using PYTHIA 6.428 [62] with the CTEQ6L1 [63] PDF set and the corresponding PERUGIA 2012 tune (P2012) [64]. The top quark mass is set to 172.5 GeV. The h_{damp} parameter, which controls the p_{T} of the first additional emission beyond the Born configuration, is set to the mass of the top quark. The main effect of this parameter is to regulate the high-p_{T} emission against which the $t\bar{t}$ system recoils [59]. The $t\bar{t}$ events are normalized to cross-sections calculated at NNLO+NNLL [65, 66] cross-section. The s- and t-channel single-top events are normalized to the NLO cross-sections [67, 68], and the Wt-channel single-top events are normalized to the NNLO+NNLL [69, 70]. Production of a top quark in association with a Z boson is generated with the MG5_aMC@NLO 2.2.1 generator at LO with CTEQ6L1 PDF set. The same PDF set and the corresponding P2012 tune is used for the parton shower, fragmentation, and the underlying event with PYTHIA 6.428. The events are normalized to LO cross section by the generator.

For the generation of $t\bar{t}$ + EW processes ($t\bar{t}+W/Z/WW$) [71], the MG5_aMC@NLO 2.2.3 generator at LO interfaced to the PYTHIA 8.186 parton-shower model is used, with up to two ($t\bar{t}+W$, $t\bar{t}+Z(\rightarrow \nu\nu/qq)$), one

($t\bar{t}+Z(\rightarrow \ell\ell)$) or no ($t\bar{t}+WW$) extra partons included in the matrix element. The tune A14 is used together with the NNPDF2.3LO PDF set. The events are normalized to their respective NLO cross-sections [72, 73]. The top quark mass is also set to 172.5 GeV.

Diboson processes (WW, WZ, ZZ) [74] are simulated using the SHERPA 2.1.1 generator. For processes with four charged leptons (4ℓ), three charged leptons and a neutrino ($3\ell+1\nu$) or two charged leptons and two neutrinos ($2\ell+2\nu$), the matrix elements contain all diagrams with four electroweak couplings, and are calculated for up to one (4ℓ, $2\ell+2\nu$) or no partons ($3\ell+1\nu$) at NLO. For processes in which one of the bosons decays hadronically and the other leptonically, matrix elements are calculated for up to one (ZZ) or no (WW, WZ) additional partons at NLO. All Diboson samples also simulate up to three additional partons at LO using the COMIX and OPENLOOPS matrix-element generators, and are merged with the SHERPA parton shower using the ME+PS@NLO prescription. In all the processes, the CT10 PDF set is used in conjunction with a dedicated parton-shower tuning developed by the authors of SHERPA. The generator cross-section are used.

The multi-jet background is generated with PYTHIA 8.186 using the A14 event tune and the NNPDF2.3LO parton distribution functions.

A summary of the SUSY signals and the SM background processes together with the MC generators, cross-section calculation orders in α_{s}, PDFs, parton shower and tunes used is given in Table 1.

Physics process	Generator	Cross-section normalization	PDF set	Parton shower	Tune
SUSY processes	MG5_aMC@NLO 2.2.2–2.3.3	NLO+NLL	NNPDF2.3LO	PYTHIA 8.186	A14
$W(\rightarrow \ell\nu)$ + jets	SHERPA 2.2.1	NNLO	NNPDF3.0NNLO	SHERPA	SHERPA default
$Z/\gamma^*(\rightarrow \ell\bar{\ell})$ + jets	SHERPA 2.2.1	NNLO	NNPDF3.0NNLO	SHERPA	SHERPA default
γ + jets	SHERPA 2.1.1	LO	CT10	SHERPA	SHERPA default
$t\bar{t}$	POWHEG-BOX v2	NNLO+NNLL	CT10	PYTHIA 6.428	PERUGIA2012
Single top (Wt-channel)	POWHEG-BOX v2	NNLO+NNLL	CT10	PYTHIA 6.428	PERUGIA2012
Single top (s-channel)	POWHEG-BOX v2	NLO	CT10	PYTHIA 6.428	PERUGIA2012
Single top (t-channel)	POWHEG-BOX v1	NLO	CT10f4	PYTHIA 6.428	PERUGIA2012
Single top (Zt-channel)	MG5_aMC@NLO 2.2.1	LO	CTEQ6L1	PYTHIA 6.428	PERUGIA2012
$t\bar{t} + W/Z/WW$	MG5_aMC@NLO 2.2.3	NLO	NNPDF2.3LO	PYTHIA 8.186	A14
WW, WZ, ZZ	SHERPA 2.1.1	NLO	CT10	SHERPA	SHERPA default
Multi-jet	PYTHIA 8.186	LO	NNPDF2.3LO	PYTHIA 8.186	A14

Table 1: The SUSY signals and the Standard Model background Monte Carlo simulation samples used in this paper. The generators, the order in α_{s} of cross-section calculations used for yield normalization, PDF sets, parton showers and tunes used for the underlying event are shown.

For all SM background samples the response of the detector to particles is modelled with a full ATLAS detector simulation [75] based on GEANT4 [76]. Signal samples are prepared using a fast simulation based on a parameterization of the performance of the ATLAS electromagnetic and hadronic calorimeters [77] and on GEANT4 elsewhere. The EVTGEN v1.2.0 program [78] is used to describe the properties of the b- and c- hadron decays in the signal samples, and the background samples except those produced with SHERPA [50].

All simulated events are overlaid with multiple pp collisions simulated with the soft QCD processes of PYTHIA 8.186 using the A2 tune [41] and the MSTW2008LO parton distribution functions [79]. The MC samples were generated with an expected pile-up distribution (multiple pp interactions in the same or neighbouring bunch-crossings) and are reweighted to match the distribution of the mean number of interactions observed in data.

4 Object reconstruction and identification

The reconstructed primary vertex of the event is required to be consistent with the luminous region and to have at least two associated tracks with $p_T > 400$ MeV. When more than one such vertex is found, the vertex with the largest $\sum p_T^2$ of the associated tracks is chosen.

Jet candidates are reconstructed using the anti-k_t jet clustering algorithm [80, 81] with a jet radius parameter of 0.4 starting from clusters of calorimeter cells [82]. The jets are corrected for energy from pile-up using the method described in Ref. [83]: a contribution equal to the product of the jet area and the median energy density of the event is subtracted from the jet energy [84]. Further corrections, referred to as the jet energy scale corrections, are derived from MC simulation and data and are used to calibrate the average energies of jets to the scale of their constituent particles [85]. Only corrected jet candidates with $p_T > 20$ GeV and $|\eta| < 2.8$ are retained. An algorithm based on boosted decision trees, 'MV2c10' [86, 87], is used to identify jets containing a b-hadron (b-jets), with an operating point corresponding to an efficiency of 77%, and rejection factors of 134 for light-quark jets and 6 for charm jets [87] for reconstructed jets with $p_T > 20$ GeV and $|\eta| < 2.5$. Candidate b-tagged jets are required to have $p_T > 50$ GeV and $|\eta| < 2.5$. Events with jets originating from detector noise and non-collision background are rejected if the jets fail to satisfy the 'LooseBad' quality criteria, or if at least one of the two leading jets with $p_T > 100$ GeV fails to satisfy the 'TightBad' quality criteria, both described in Ref. [88]. The application of these selection requirements affects less than 1% of the events used in the search. In order to reduce the number of jets coming from pile-up, a significant fraction of the tracks associated with each jet must have an origin compatible with the primary vertex, as defined by the jet vertex tagger (JVT) output [89]. The requirement JVT > 0.59 is only applied to jets with $p_T < 60$ GeV and $|\eta| < 2.4$.

Two different classes of reconstructed lepton candidates (electrons or muons) are used in the analyses presented here. When selecting samples for the search, events containing a 'baseline' electron or muon are rejected. The selections applied to identify baseline leptons are designed to maximize the efficiency with which W+jets and top quark background events are rejected. When selecting 'control region' samples for the purpose of estimating residual W+jets and top quark backgrounds, additional requirements are applied to leptons to ensure greater purity of these backgrounds. These leptons are referred to as 'high-purity' leptons below and form a subset of the baseline leptons.

Baseline muon candidates are formed by combining information from the muon spectrometer and inner tracking detectors as described in Ref. [90] and are required to have $p_T > 7$ GeV and $|\eta| < 2.7$. High-purity muon candidates must additionally have $|\eta| < 2.4$, the significance of the transverse impact parameter with respect to the primary vertex $|d_0^{PV}|/\sigma(d_0^{PV}) < 3$, the longitudinal impact parameter with respect to the primary vertex $|z_0^{PV}\sin(\theta)| < 0.5$ mm, and to satisfy 'GradientLoose' isolation requirements described in Ref. [90] which rely on tracking-based and calorimeter-based variables and implement a set of η- and p_T-dependent criteria. The leading, high-purity muon, is also required to have $p_T > 27$ GeV.

Baseline electron candidates are reconstructed from an isolated electromagnetic calorimeter energy deposit matched to an ID track and are required to have $p_T > 7$ GeV, $|\eta| < 2.47$, and to satisfy 'Loose' likelihood-based identification criteria described in Ref. [91]. High-purity electron candidates additionally must satisfy 'Tight' selection criteria described in Ref. [91], and the leading electron must have $p_T > 27$ GeV. They are also required to have $|d_0^{PV}|/\sigma(d_0^{PV}) < 5$, $|z_0^{PV}\sin(\theta)| < 0.5$ mm, and to satisfy similar isolation requirements as those applied to high-purity muons [91].

After the selections described above, ambiguities between candidate jets with $|\eta| < 2.8$ and leptons are resolved as follows: first, any such jet candidate which is not tagged as b-jet, lying within a distance

$\Delta R \equiv \sqrt{(\Delta y)^2 + (\Delta \phi)^2} = 0.2$ of a baseline electron is discarded. If a jet candidate is b-tagged, the object is interpreted as a jet and the overlapping electron is ignored. Additionally, if a baseline electron (muon) and a jet passing the JVT selection described above are found within $0.2 \leq \Delta R < 0.4$ ($< \min(0.4, 0.04 + 10 \text{ GeV}/p_\text{T}^\mu)$), the object is interpreted as a jet and the nearby electron (muon) candidate is discarded. Finally, if a baseline muon and jet are found within $\Delta R < 0.2$, the object is treated as a muon and the overlapping jet is ignored. In this case, the jet must satisfy $N_\text{trk} < 3$, where N_trk refers to the number of tracks with $p_\text{T} > 500$ MeV that are associated to the jet. These selection criteria reject jets consistent with final state radiation or hard bremsstrahlung.

Additional ambiguities between electrons and muons in a jet, originating from the decays of hadrons, are resolved to avoid double counting and/or remove non-isolated leptons: the electron is discarded if a baseline electron and a baseline muon share the same ID track.

The measurement of the missing transverse momentum vector $\vec{E}_\text{T}^\text{miss}$ (and its magnitude E_T^miss) is based on the calibrated transverse momenta of all electron, muon, and jet candidates and all tracks originating from the primary vertex and not associated with such objects [92].

Reconstructed photons are not used in the signal-event selection, but in the control region used to constrain the Z+jets background, as explained in Section 8. Photon candidates are required to satisfy $p_\text{T} > 150$ GeV and $|\eta| < 2.37$, photon shower shape and electron rejection criteria, and to be isolated [93]. Ambiguities between candidate jets and photons (when used in the event selection) are resolved by discarding any jet candidates lying within $\Delta R = 0.4$ of a photon candidate. Additional selections to remove ambiguities between electrons or muons and photons are applied such that a photon is discarded if it is within $\Delta R = 0.4$ of a baseline electron or muon.

Initial jet-finding is extended using an approach called jet re-clustering [94]. This allows the use of larger-radius jet algorithms while maintaining the calibrations and systematic uncertainties associated with the input jets. Jets with a radius parameter 0.4 described above surviving the resolution of ambiguities and having $p_\text{T} > 25$ GeV are used as input to an anti-k_t algorithm with a jet radius parameter 1.0. A grooming scheme called "re-clustered jet trimming" is applied to remove any small radius jet constituent j of a large-radius re-clustered jet J if $p_\text{T}^j < f_\text{cut} \times p_\text{T}^J$ where the parameter f_cut is set to be 0.05.

Corrections derived from data control samples are applied to account for differences between data and simulation for the lepton and photon trigger and reconstruction efficiencies, the lepton momentum/energy scale and resolution, and for the efficiency and mis-tag rate of the b-tagging algorithm.

5 Analysis strategy and background prediction

This section summarizes the common analysis strategy and statistical techniques that are employed in the searches presented in this paper.

To search for a possible signal, selections are defined to enhance the expected signal yield relative to the SM backgrounds. Signal regions (SRs) are defined using the Monte Carlo simulation of SUSY signals and the SM background processes. They are optimized to maximize the expected sensitivity to each model considered. To estimate the SM backgrounds in an accurate and robust fashion, control regions (CRs) are defined for each of the signal regions. They are chosen to be orthogonal to the SR selections in order to provide independent data samples enriched in particular background sources, and are used to normalize the background MC simulation. The CR selections are optimized to have negligible SUSY

signal contamination for the models near the previously excluded boundary [11], while minimizing the systematic uncertainties arising from the extrapolation of the CR event yields to estimate backgrounds in the SR. Cross-checks of the background estimates are performed with data in several validation regions (VRs) selected with requirements such that these regions do not overlap with the CR and SR selections, and also have a low expected signal contamination.

In order to ensure sensitivity to the variety of squark and gluino production signals targeted in this search, a collection of SRs is considered. Each of the SR selection requirements are optimized to exploit expected differences in masses, kinematics, and jet multiplicities, and each represents its own independent counting experiment. Two different approaches are used in defining these SRs, with Meff-based and RJR-based selection criteria used in these regions described Sections 7.1 and 7.2, respectively. While these two approaches for defining SRs are not entirely orthogonal, in that they sometimes target the same signals signals, they are complementary because of both differences in selected event populations and qualitative strategy for balancing signal-to-background and systematic uncertainties. A discussion of differences in these approaches is provided in Section 7.3.

To extract the final results, three different classes of likelihood fits are employed: background-only, model-independent and model-dependent fits [95]. A background-only fit is used to estimate the background yields in each SR. The fit is performed using the observed event yields of the CRs associated with the SR as the only constraints, but not the yields of the SR itself. It is assumed that signal events from physics beyond the Standard Model (BSM) do not contribute to these CR yields. The scale factors ($\mu_{W+\text{jets}}$, $\mu_{Z+\text{jets}}$, μ_{Top}) represent the normalization of background components relative to MC expectations, and are determined in a fit to all the CRs associated to a SR. The expected background in the SR is based on the yields predicted by simulation for W/Z+jets and background processes containing on-shell top quarks, corrected by the scale factors derived from the fit. In case of multi-jet background, the estimate is based on the data-driven method described in Section 8. The systematic uncertainties and the MC statistical uncertainties in the expected values are included in the fit as nuisance parameters which are constrained by Gaussian distributions with widths corresponding to the sizes of the uncertainties considered and by Poisson distributions, respectively. The background-only fit is also used to estimate the background event yields in the VRs.

A model-independent fit is used to quantify the agreement between background predictions and observed yields and to set upper limits on the number of BSM signal events in each SR. This fit proceeds in the same way as the background-only fit, except that the signal contributions in both the SR and the CRs are taken into account. The observed and expected upper limits at 95% confidence level (CL) on the number of events from BSM phenomena for each signal region (S^{95}_{obs} and S^{95}_{exp}) are derived using the CL_s prescription [96], neglecting any possible signal contamination in the control regions. These limits, when normalized by the integrated luminosity of the data sample, may be interpreted as upper limits on the visible cross-section of BSM physics ($\langle\epsilon\sigma\rangle^{95}_{\text{obs}}$), where the visible cross-section is defined as the product of production cross-section, acceptance and efficiency. The model-independent fit is also used to compute the one-sided p-value (p_0) of the background-only hypothesis, which quantifies the statistical significance of an excess.

Finally, a model-dependent fit is used to set exclusion limits on the signal cross-sections for specific SUSY models. Such a fit proceeds in the same way as the model-independent fit, except that both the signal yield in the signal region and the signal contamination in the CRs are taken into account. Correlations between signal and background systematic uncertainties are taken into account where appropriate. Signal-yield systematic uncertainties due to detector effects and the theoretical uncertainties in the signal acceptance are included in the fit.

9

6 The Recursive Jigsaw Reconstruction technique

The Recusive Jigsaw Reconstruction (RJR) technique [12, 13] is a method for defining kinematic variables on an event-by-event level. While it is straightforward to fully describe an event's underlying kinematic features when all objects are fully reconstructed, events involving invisible weakly interacting particles present a challenge, as the loss of information from escaping particles constrains the kinematic variable construction to take place in the lab frame instead of the more physically natural frames of the hypothesized decays. The RJR method partially mitigates this loss of information by determining approximations of the rest frames of intermediate particle states in each events. This reconstructed view of the event gives rise to a natural basis of kinematic observables, calculated by evaluating the momenta and energy of different objects in these reference frames.
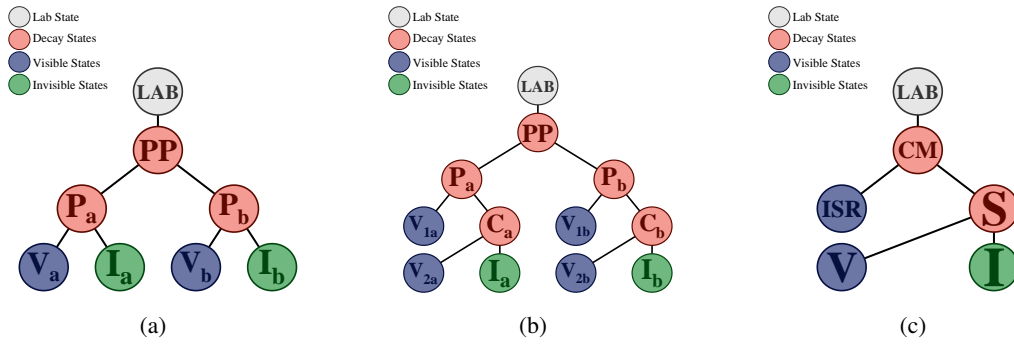

Figure 2: (a) Inclusive strong sparticle production decay tree. Two sparticles (P_a and P_b) are non-resonantly pair-produced with each decaying to one or more visible particles (V_a and V_b) which are reconstructed in the detector, and two systems of invisible particles (I_a and I_b) whose four-momenta are only partially constrained. (b) An additional level of decays can be added when requiring more than two visible objects. This tree is particularly useful for the search for gluino pair-production described in the text. (c) Strong sparticle production with ISR decay tree for use with small mass-splitting spectra. A signal sparticle system S decaying to a set of visible momenta V and invisible momentum I recoils off of a jet radiation system ISR.

All jets with $p_T^{\text{jet}} > 50$ GeV and $|\eta_{\text{jet}}| < 2.8$ and the E_T^{miss} are used as input to the RJR algorithm. Motivated by searches for strong production of sparticles in R-parity conserving models, a decay tree, shown in Figure 2(a), is used in the analysis of events. Each event is evaluated as if two sparticles (the intermediate states P_a and P_b) were produced and then decayed to the particles observed in our detector (the collections V_a and V_b). The benchmark signal models probed in this search give rise to signal events with at least two weakly-interacting particles associated with two systems of particles (I_a and I_b), the respective children of the initially produced sparticles.

This decay tree includes several kinematic and combinatoric unknowns. In the final state with no leptons, the objects observed in the detector are exclusively jets and it is necessary to decide how to partition these jets into the two groups V_a and V_b in order to calculate the observables associated with the decay tree. In this paper, the grouping that minimizes the masses of the four-vector sum of group constituents is chosen.

More explicitly, the collection of reconstructed jet four-vectors, $V \equiv \{p_i\}$ and their four-vector sum p_V are considered. Each of the four-momenta is evaluated in the rest-frame of p_V (V-frame) and different

partitionings of these jets $V_i = \{p_1, \cdots, p_{N_i}\}$ are considered such that $V_a \bigcap V_b = 0$ and $V_a \bigcup V_b = V$. For each partition, the sum of four-vectors $p_{V_i}^V = \sum_{j=1}^{N_i} p_j^V$ is calculated and the combination is chosen that maximizes the sum of momentum of the two groups, $|\vec{p}_{V_a}^V| + |\vec{p}_{V_b}^V|$. The axis that this partition implicitly defines in the V rest-frame is equivalent to the thrust-axis of the jets, and the masses $M_{V_i} = \sqrt{p_{V_i}^2}$ are simultaneously minimized. These two groups are called "jet hemispheres."

The remaining unknowns in the event are associated with the two collections of weakly interacting particles: their masses, longitudinal momenta and information as how the two groups contribute to the $\vec{E}_T^{\text{miss}}$. The RJR algorithm guesses these unknowns through subsequent minimizations of the intermediate particle masses appearing in the decay tree. In each of these newly constructed rest frames, all relevant momenta are defined and can be used to construct any variable – multi-object invariant masses, angles between objects, etc. The primary energy-scale-sensitive observables used in the search presented here are a suite of variables denoted by H. These H variables derive their name from H_T, the scalar sum of visible transverse momenta. However, in contrast to H_T, these H variables are constructed with aggregate momenta, including contributions from the invisible four-momenta, and are not necessarily evaluated in the lab frame, nor only in the transverse plane.

The H variables are labeled with a superscript F and two subscripts n and m, $H_{n,m}^F$. The F represents the rest frame in which the momenta are evaluated. In this analysis, this may be the lab frame, the proxy frame for the sparticle-sparticle frame PP, or the proxy frame for an individual sparticle's rest frame P. The subscripts n and m represent the number of visible and invisible momentum vectors considered, respectively. This means given the number of visible momentum vectors in the frame, these will be summed together until there remain only n distinct vectors. The choice for which vectors are summed is made by finding jets nearest in phase space, performed using the minimization procedure described above. The same is done for the invisible system into m vectors. For events with fewer than n visible objects, the sum will only run over the available vectors. The additional subscript T can denote a transverse version of the variable where the transverse plane is defined with respect to the velocity of the frame F. In practice, this is similar to the plane transverse to the beam-line.

The variables that are used to define the signal and control regions are listed below. As few requirements are placed on dimensionful variables as possible, in order to increase the generality of the signal regions' sensitivity. Additional discrimination is acheived through a minimal set of dimensionless variable requirements with selections imposed on unitless quantities exploiting common mass-independent features of the signals considered.

To select signal events in models with squark-pair production, the following variables are used:

- $H_{1,1}^{PP}$: scale variable as described above. Measures the momentum of missing particles in the PP frame and behaves similarly to E_T^{miss}.

- $H_{T\,2,1}^{PP}$: scale variable as described above. Behaves similarly to effective mass, m_{eff} (defined as the scalar sum of the transverse momenta of the two leading jets and E_T^{miss}) for squark-pair production signals with two-jet final states.

- $H_{1,1}^{PP}/H_{2,1}^{PP}$: provides additional information in testing the balance of the information provided by the two scale cuts, where in the denominator the $H_{2,1}^{PP}$ is no longer solely transverse. This provides an excellent handle against imbalanced events where the large scale is dominated by a particular object p_T or by high E_T^{miss}.

- $p_z^{\text{lab}}/(p_z^{\text{lab}} + H_{\text{T}\,2,1}^{\text{PP}})$: compares the z-momentum of the lab frame to the overall transverse scale variable considered. This variable tests for significant boost in the z direction.

- $p_{\text{Tj2}}^{\text{PP}}/H_{\text{T}\,2,1}^{\text{PP}}$: represents the fraction of the overall scale variable that is due to the second highest p_{T} jet (in the PP frame, $p_{\text{Tj2}}^{\text{PP}}$) in the event, with small values generally more background-like.

For signal topologies with higher jet multiplicities, there is the option to exploit the internal structure of the hemispheres by using a decay tree with an additional decay. For gluino-pair production, the tree shown in Figure 2(b) can be used and the variables used by this search are:

- $H_{1,1}^{\text{PP}}$: described above.

- $H_{\text{T}\,4,1}^{\text{PP}}$: analogous to the transverse scale variable described above but more appropriate for four-jet final states expected from gluino-pair production.

- $H_{1,1}^{\text{PP}}/H_{4,1}^{\text{PP}}$: analogous to $H_{1,1}^{\text{PP}}/H_{2,1}^{\text{PP}}$ for the squark search.

- $H_{\text{T}\,4,1}^{\text{PP}}/H_{4,1}^{\text{PP}}$: a measure of the fraction of the momentum that lies in the transverse plane.

- $p_z^{\text{lab}}/(p_z^{\text{lab}} + H_{\text{T}\,4,1}^{\text{PP}})$: analogous to $p_z^{\text{lab}}/(p_z^{\text{lab}} + H_{\text{T}\,2,1}^{\text{PP}})$ above.

- $\min_i (p_{\text{Tj2i}}^{\text{PP}}/H_{\text{T}\,2,1i}^{\text{PP}})$: represents the fraction of a hemisphere's overall scale due to the second highest p_{T} jet (in the PP frame) in each hemisphere. The minimum value between the two hemispheres is used, corresponding to the index i.

- $\max_i (H_{1,0}^{\text{P}_i}/H_{2,0}^{\text{P}_i})$: testing balance of solely the jets momentum in a given hemisphere's approximate sparticle rest frame (P_i, index i indicating each hemisphere) allows an additional handle against a small but otherwise signal-like subset of vector boson with associated jets background events.

In order to reject events where the $E_{\text{T}}^{\text{miss}}$ results from mis-measurements of jets, the $E_{\text{T}}^{\text{miss}}$ is associated with one or more jets using a transverse clustering scheme, identifying those jets which are closest in phase-space. The variable Δ_{QCD} considers the magnitude of $\vec{E}_{\text{T}}^{\text{miss}}$, the transverse momentum of the associated jets, along with the azimuthal angle between the two, in order to quantify the likelihood that mis-measurements of these jets were responsible for the $E_{\text{T}}^{\text{miss}}$. Multi-jet events with severe jet mis-measurements tend to have Δ_{QCD} values between [-1,0] while events with $E_{\text{T}}^{\text{miss}}$ from weakly-interacting particles prefer [0,1]. The variable is defined as the signed asymmetry between

- the transverse momentum of the associated jet system that projects onto the direction of the $E_{\text{T}}^{\text{miss}}$ system normalized to this value summed with the $E_{\text{T}}^{\text{miss}}$ and

- the normalized angle between this jet system and the vectorial sum of it and the $E_{\text{T}}^{\text{miss}}$ system.

In addition to trying to resolve the entirety of the signal event, it can be useful for sparticle spectra with smaller mass splittings and lower intrinsic $E_{\text{T}}^{\text{miss}}$ to instead select for a partially-resolved sparticle system recoiling off of a high-p_{T} jet from initial state radiation (ISR). To target such topologies, a separate tree targeting compressed spectra can be seen in Figure 2(c). This tree is somewhat simpler and attempts to identify visible (V) and invisible (I) systems that are the result of an intermediate state corresponding to the system of sparticles and their decay products (S). This signal system is required to recoil off of a system of visible momenta associated with the ISR. This tree yields a slightly different set of variables:

- $p_{\text{TS}}^{\text{CM}}$: the magnitude of the vector-summed transverse momenta of all S-associated jets and $E_{\text{T}}^{\text{miss}}$ evaluated in the CM frame.

- $R_{\mathrm{ISR}} \equiv \vec{p}_{\mathrm{I}}^{\,\mathrm{CM}} \cdot \hat{p}_{\mathrm{TS}}^{\,\mathrm{CM}} / p_{\mathrm{TS}}^{\mathrm{CM}}$: serves as a proxy for $m_{\tilde{\chi}}/m_{\tilde{p}}$. This is the fraction of the boost of the S system that is carried by its invisible system I. As the $|p_{\mathrm{TS}}^{\mathrm{ISR}}|$ is increased it becomes increasingly hard for backgrounds to possess a large value in this ratio - a feature exhibited by compressed signals.

- M_{TS}: the transverse mass of the S system.

- $N_{\mathrm{jet}}^{\mathrm{V}}$: number of jets assigned to the visible system (V) and not associated with the ISR system.

- $\Delta\phi_{\mathrm{ISR,I}}$: This is the opening angle between the ISR system and the invisible system in the lab frame.

7 Event selection and signal regions definitions

Following the object reconstruction described in Section 4, in both searches documented here events are discarded if a baseline electron or muon with $p_{\mathrm{T}} > 7$ GeV remains, or if they contain a jet failing to satisfy quality selection criteria designed to suppress detector noise and non-collision backgrounds (described in Section 4). Events are rejected if no jets with $p_{\mathrm{T}} > 50$ GeV are found. The remaining events are then analyzed in two complementary searches, both of which require the presence of jets and significant missing transverse momentum. The selections in the two searches are designed to be generic enough to ensure sensitivity in a broad set of models with jets and $E_{\mathrm{T}}^{\mathrm{miss}}$ in the final state.

In order to maximize the sensitivity in the $(m_{\tilde{g}}, m_{\tilde{q}})$ plane, a variety of signal regions are defined. Squarks typically generate at least one jet in their decays, for instance through $\tilde{q} \rightarrow q\tilde{\chi}_1^0$, while gluinos typically generate at least two jets, for instance through $\tilde{g} \rightarrow q\bar{q}\tilde{\chi}_1^0$. Processes contributing to $\tilde{q}\tilde{q}$ and $\tilde{g}\tilde{g}$ final states therefore lead to events containing at least two or four jets, respectively. Decays of heavy SUSY and SM particles produced in longer $\tilde{q}$ and $\tilde{g}$ decay cascades (e.g. $\tilde{\chi}_1^\pm \rightarrow qq'\tilde{\chi}_1^0$) tend to further increase the jet multiplicity in the final state. To target different scenarios, signal regions with different jet multiplicity requirements (in the case of Meff-based search) or different decay trees (in the case of RJR-based search) are assumed. The optimized signal regions used in both searches are summarized in the following.

7.1 The jets+$E_{\mathrm{T}}^{\mathrm{miss}}$ Meff-based search

Due to the high mass scale expected for the SUSY models considered in this study, the 'effective mass', m_{eff} [97], is a powerful discriminant between the signal and SM backgrounds. When selecting events with at least N_{j} jets, $m_{\mathrm{eff}}(N_{\mathrm{j}})$ is defined to be the scalar sum of the transverse momenta of the leading N_{j} jets and $E_{\mathrm{T}}^{\mathrm{miss}}$. Requirements placed on $m_{\mathrm{eff}}(N_{\mathrm{j}})$ and $E_{\mathrm{T}}^{\mathrm{miss}}$ form the basis of the Meff-based search by strongly suppressing the multi-jet background where jet energy mismeasurement generates missing transverse momentum. The final signal selection uses a requirement on $m_{\mathrm{eff}}(\mathrm{incl.})$, which sums over all jets with $p_{\mathrm{T}} > 50$ GeV and $E_{\mathrm{T}}^{\mathrm{miss}}$ to suppress SM backgrounds which tend to have low jet multiplicity.

Twenty-four inclusive SRs characterized by increasing the minimum jet multiplicity, from two to six, are defined in Table 2: eight regions target models characterized by the squark-pair production with the direct decay of squarks, seven regions target models with gluino-pair production followed by the direct decay of gluinos and nine regions target squark-pair or gluino-pair production followed by the one-step decay of squark/gluino via an intermediate chargino or neutralino. Signal regions requiring the same jet-multiplicity are distinguished by increasing the threshold of the $m_{\mathrm{eff}}(\mathrm{incl.})$ and $E_{\mathrm{T}}^{\mathrm{miss}}/m_{\mathrm{eff}}(N_{\mathrm{j}})$ or

$E_T^{\text{miss}}/\sqrt{H_T}$ requirements. This ensures the sensitivity to a range of sparticle masses for each decay mode. All signal regions corresponding to the Meff-based approach are labelled with the prefix 'Meff'.

In each region, different thresholds are applied on jet momenta and pseudorapidities. These thresholds are defined to reduce SM background while keeping high efficiency for targeted signal events which tend to have hard jets in the central region.

Requirements on $\Delta\phi(\text{jet}, \vec{E}_T^{\text{miss}})_{\text{min}}$, which is defined to be the smallest azimuthal separation between $\vec{E}_T^{\text{miss}}$ and the momenta of any of the reconstructed jets with $p_T > 50$ GeV, and $E_T^{\text{miss}}/m_{\text{eff}}(N_j)$, are designed to reduce the background from multi-jet processes. For the 2-jet SRs which are optimized for squark-pair production followed by the direct decay of squarks and Meff-5j-2600, the selection requires $\Delta\phi(\text{jet}_{1,2,(3)}, \vec{E}_T^{\text{miss}})_{\text{min}} > 0.8$ using up to three leading jets (if present in the event), while in SRs with higher jet multiplicities the requirement $\Delta\phi(\text{jet}_{1,2,(3)}, \vec{E}_T^{\text{miss}})_{\text{min}} > 0.4$ is used. Meff-2jB-1600/2400 which require two large-radius jets, $\Delta\phi(\text{jet}_{1,2,(3)}, \vec{E}_T^{\text{miss}})_{\text{min}} > 0.6$ is used. For the SRs requiring at least four, five or six jets in the final state, or in the case that more than three jets are present in 2-jet or 3-jet SRs, an additional requirement on $\Delta\phi(\text{jet}_{i>3}, \vec{E}_T^{\text{miss}})_{\text{min}} > 0.4$ (or 0.2 depending on SRs) is applied to all jets with $p_T > 50$ GeV.

In the 2-jet and 3-jet SRs, Meff-5j-2000/2600 and Meff-2jB-1600/2400, the requirement on $E_T^{\text{miss}}/m_{\text{eff}}(N_j)$ is replaced by a requirement on $E_T^{\text{miss}}/\sqrt{H_T}$ (where H_T is defined as the scalar sum of the transverse momenta of all jets), which is found to lead to enhanced sensitivity to models characterized by $\tilde{q}\tilde{q}$ production. In the other regions with at least four jets in the final state, jets from signal processes distribute isotropically. Additional suppression of background processes is based on the aplanarity variable, which is defined as $A = 3/2\lambda_3$, where λ_3 is the smallest eigenvalue of the normalized momentum tensor of the jets [98].

Two signal regions, Meff-2jB-1600/2400, optimized for one-step decay models are designed to improve the sensitivity to models with the cascade squark decay via $\tilde{\chi}^\pm$ to $qW\tilde{\chi}_1^0$ (Figure 1(b)) or gluino decay via $\tilde{\chi}^\pm$ to $qqW\tilde{\chi}_1^0$ (or $qqZ\tilde{\chi}_1^0$) (Figure 1(e, f)), in cases where the $\tilde{\chi}^\pm$ is nearly degenerate in mass with the squarks or the gluino. These signal regions place additional requirements on the mass of the large-radius jets to select the candidate hadronically decaying W or Z bosons which, due to the small mass difference between the parent SUSY particles and intermediate chargino or neutralino, can have significant transverse momentum and appear as a single high-mass jet.

The selection criteria of all the Meff-based signal regions are summarized in Table 2.

Targeted signal	$\tilde{q}\tilde{q}, \tilde{q} \to q\tilde{\chi}_1^0$							
Requirement	Signal Region [**Meff-**]							
	2j-1200	**2j-1600**	**2j-2000**	**2j-2400**	**2j-2800**	**2j-3600**	**2j-2100**	**3j-1300**
E_T^{miss} [GeV] >	250							
$p_T(j_1)$ [GeV] >	250	300	350				600	700
$p_T(j_2)$ [GeV] >	250	300	350				50	
$p_T(j_3)$ [GeV] >	–							50
$\|\eta(j_{1,2})\|$ <	0.8	1.2					–	
$\Delta\phi(\mathrm{jet}_{1,2,(3)}, \vec{E}_T^{miss})_{min}$ >	0.8						0.4	
$\Delta\phi(\mathrm{jet}_{i>3}, \vec{E}_T^{miss})_{min}$ >	0.4						0.2	
$E_T^{miss}/\sqrt{H_T}$ [GeV$^{1/2}$] >	14	18					26	16
$m_{eff}(\mathrm{incl.})$ [GeV] >	1200	1600	2000	2400	2800	3600	2100	1300

Targeted signal	$\tilde{g}\tilde{g}, \tilde{g} \to q\bar{q}\tilde{\chi}_1^0$						
Requirement	Signal Region [**Meff-**]						
	4j-1000	**4j-1400**	**4j-1800**	**4j-2200**	**4j-2600**	**4j-3000**	**5j-1700**
E_T^{miss} [GeV] >	250						
$p_T(j_1)$ [GeV] >	200						700
$p_T(j_4)$ [GeV] >	100				150		50
$p_T(j_5)$ [GeV] >	–						50
$\|\eta(j_{1,2,3,4})\|$ <	1.2	2.0					–
$\Delta\phi(\mathrm{jet}_{1,2,(3)}, \vec{E}_T^{miss})_{min}$ >	0.4						
$\Delta\phi(\mathrm{jet}_{i>3}, \vec{E}_T^{miss})_{min}$ >	0.4						0.2
$E_T^{miss}/m_{eff}(N_j)$ >	0.3	0.25			0.2		0.3
Aplanarity >	0.04						–
$m_{eff}(\mathrm{incl.})$ [GeV] >	1000	1400	1800	2200	2600	3000	1700

Targeted signal	$\tilde{g}\tilde{g}, \tilde{g} \to q\bar{q}W\tilde{\chi}_1^0$ and $\tilde{q}\tilde{q}, \tilde{q} \to qW\tilde{\chi}_1^0$						
Requirement	Signal Region [**Meff-**]						
	5j-1600	**5j-2000**	**5j-2600**	**6j-1200**	**6j-1800**	**6j-2200**	**6j-2600**
E_T^{miss} [GeV] >	250						
$p_T(j_1)$ [GeV] >	200						
$p_T(j_6)$ [GeV] >	50			100			
$\|\eta(j_{1,...,6})\|$ <	–			2.0		–	
$\Delta\phi(\mathrm{jet}_{1,2,(3)}, \vec{E}_T^{miss})_{min}$ >	0.4		0.8	0.4			
$\Delta\phi(\mathrm{jet}_{i>3}, \vec{E}_T^{miss})_{min}$ >	0.2	0.4		0.2			
$E_T^{miss}/m_{eff}(N_j)$ >	0.15	–		0.25	0.2		0.15
$E_T^{miss}/\sqrt{H_T}$ [GeV$^{1/2}$] >	–	15	18	–			
Aplanarity >	0.08	–		0.04		0.08	
$m_{eff}(\mathrm{incl.})$ [GeV] >	1600	2000	2600	1200	1800	2200	2600

Targeted signal	$\tilde{g}\tilde{g}, \tilde{g} \to q\bar{q}W\tilde{\chi}_1^0$ and $\tilde{q}\tilde{q}, \tilde{q} \to qW\tilde{\chi}_1^0$	
Requirement	Signal Region	
	Meff-2jB-1600	**Meff-2jB-2400**
E_T^{miss} [GeV] >	250	
$p_T(\text{Large-R } j_1)$ [GeV] >	200	
$p_T(\text{Large-R } j_2)$ [GeV] >	200	
$m(\text{Large-R } j_1)$ [GeV]	[60,110]	
$m(\text{Large-R } j_2)$ [GeV]	[60,110]	
$\Delta\phi(\mathrm{jet}_{1,2,(3)}, \vec{E}_T^{miss})_{min}$ >	0.6	
$\Delta\phi(\mathrm{jet}_{i>3}, \vec{E}_T^{miss})_{min}$ >	0.4	
$E_T^{miss}/\sqrt{H_T}$ [GeV$^{1/2}$] >	20	
$m_{eff}(\mathrm{incl.})$ [GeV] >	1600	2400

Table 2: Selection criteria and targeted signal model from Fig. 1 used to define signal regions in the Meff-based search, indicated by the prefix 'Meff'. The first block of SRs targets Fig. 1 (a), the second block of SRs targets Fig. 1 (d). The third and fourth blocks of SRs targets Fig. 1 (b) and (e). Each SR is labelled with the inclusive jet multiplicity considered ('2j', '3j' etc.) together with the degree of background rejection. The latter is denoted by the value corresponding to the m_{eff} cut. The $E_T^{miss}/m_{eff}(N_j)$ cut in any N_j-jet channel uses a value of m_{eff} constructed from only the leading N_j jets ($m_{eff}(N_j)$). However, the final $m_{eff}(\mathrm{incl.})$ selection, which is used to define the signal regions, includes all jets with $p_T > 50$ GeV. Large-radius re-clustered jets are denoted as Large-R j.

7.2 The jets+E_T^miss RJR-based search

As with the Meff-based search, various signal regions are defined in the RJR-based approach to be most sensitive to a variety of potential SUSY signals. It is chosen to limit the number of dimensionful variables to only two when defining the signal regions targeting models with the gluino- and squark-pair production. The different types of signals are grouped according to sparticle mass splittings, each with dedicated optimizations. The two chosen scale variables are $H_{1,1}^\text{PP}$ and either $H_{\text{T}\,2,1}^\text{PP}$ (for models targeting squark-pair production) or $H_{\text{T}\,4,1}^\text{PP}$ (for models targeting gluino-pair production). These serve to select events with large missing momentum and a high collective scale of reconstructed visible objects. In order to further suppress SM backgrounds, a variety of additional constraints on dimensionless variables are imposed.

In general, the procedure is such that, as the mass splitting between parent sparticle and LSP increases, the criteria applied to the scale variables are tightened, while the criteria on dimensionless variables are loosened. In searching for the squark-pair production, the overall balance of the events is studied with $H_{1,1}^\text{PP}/H_{2,1}^\text{PP}$. The range selected in this ratio rejects those events where the missing transverse momentum dominates the scale (upper requirement) and to ensure sufficient balance between the scales (lower requirement). The selection on the $p_{\text{T}j2}^\text{PP}/H_{\text{T}\,2,1}^\text{PP}$ ratio serves to ensure that each of the jets contributes to the overall scale significantly. This particular ratio is a powerful criterion against imbalanced events with V+jets, where one of the jets has a much higher momentum than the sub-leading jet.

For gluino-pair produced signals, the same principles are followed. Tight requirements are placed on $H_{1,1}^\text{PP}/H_{4,1}^\text{PP}$ and $H_{\text{T}\,4,1}^\text{PP}/H_{4,1}^\text{PP}$ to target scenarios with compressed spectra. A selection is applied on the ratio $p_{\text{z, PP}}^\text{lab}/\left(p_{\text{z, PP}}^\text{lab} + H_{\text{T}\,4,1}^\text{PP}\right)$ to test the size of the z-component relative to the overall scale, requiring that it should be small. A lower threshold is placed on the ratio of the second jet divided by the scale of the hemisphere. This provides a very strong constraint against events where the two hemispheres are well-balanced but one of the jets dominates the scale variable contribution. In order to reject events where the E_T^miss results from mis-measurements of jets a requirement on the variable Δ_QCD is applied, rejecting events where this is deemed likely.

Additionally, separate SRs are defined for models with compressed spectra. Following the pattern of successive SRs targeting larger mass-splitting scenarios, several regions designed to be sensitive to various mass-splittings utilize the ISR-boosted compressed decay tree described in Section 6. These regions target mass-splittings from roughly 25 GeV to 200 GeV.

The selection criteria of the resulting nineteen signal regions are summarized in Table 3. The entries for $|\eta_{j1,j2}|$ and $|\eta_{j1,2,a,b}|$ correspond to maximum requirements on the pseudorapidities of the leading two jets in each event and the leading two jets in each hemisphere a/b, respectively, while $|\eta_{jV}|$ corresponds to the jets associated with the system V. All signal regions included in the RJR-based search have 'RJR' prefix.

Targeted signal	$\tilde{g}\tilde{g}, \tilde{g} \to q\tilde{\chi}_1^0$			
Requirement	Signal Region			
	RJR-S1	**RJR-S2**	**RJR-S3**	**RJR-S4**
$H_{1,1}^{PP}/H_{2,1}^{PP} \geq$	0.55	0.5	0.45	-
$H_{1,1}^{PP}/H_{2,1}^{PP} \leq$	0.9	0.95	0.98	-
$p_{Tj2}^{PP}/H_{T\,2,1}^{PP} \geq$	0.16	0.14	0.13	0.13
$|\eta_{j1,j2}| \leq$	0.8	1.1	1.4	2.8
$\Delta_{QCD} \geq$	0.1	0.05	0.025	0
$p_{PP,\,T}^{lab}/\left(p_{PP,\,T}^{lab}+H_{T\,2,1}^{PP}\right) \leq$	0.08			

	RJR-S1a	**RJR-S1b**	**RJR-S2a**	**RJR-S2b**	**RJR-S3a**	**RJR-S3b**	**RJR-S4**
$H_{T\,2,1}^{PP}$ [GeV] $>$	1000	1200	1400	1600	1800	2100	2400
$H_{1,1}^{PP}$ [GeV] $>$	800	1000	1200	1400	1700	1900	2100

Targeted signal	$\tilde{g}\tilde{g}, \tilde{g} \to q\bar{q}\tilde{\chi}_1^0$			
Requirement	Signal Region			
	RJR-G1	**RJR-G2**	**RJR-G3**	**RJR-G4**
$H_{1,1}^{PP}/H_{4,1}^{PP} \geq$	0.45	0.3	0.2	-
$H_{T\,4,1}^{PP}/H_{4,1}^{PP} \geq$	0.7	0.7	0.65	0.65
$\min\left(p_{Tj2i}^{PP}/H_{T\,2,1\,i}^{PP}\right) \geq$	0.12	0.1	0.08	0.07
$\max\left(H_{1,\,0}^{Pi}/H_{2,\,0}^{Pi}\right) \leq$	0.96	0.97	0.98	0.98
$|\eta_{j1,2,a,b}| \leq$	1.4	2.0	2.4	2.8
$\Delta_{QCD} \geq$	0.05	0.025	0	0
$p_{z,\,PP}^{lab}/\left(p_{z,\,PP}^{lab}+H_{T\,4,1}^{PP}\right) \leq$	0.5	0.55	0.6	0.65
$p_{PP,\,T}^{lab}/\left(p_{PP,\,T}^{lab}+H_{T\,4,1}^{PP}\right) \leq$	0.08			

	RJR-G1a	**RJR-G1b**	**RJR-G2a**	**RJR-G2b**	**RJR-G3a**	**RJR-G3b**	**RJR-G4**
$H_{T\,4,1}^{PP}$ [GeV] $>$	1200	1400	1600	2000	2400	2800	3000
$H_{1,1}^{PP}$ [GeV] $>$	700		800		900		1000

Targeted signal	compressed spectra in $\tilde{g}\tilde{g}\ (\tilde{g} \to q\tilde{\chi}_1^0)$; $\tilde{g}\tilde{g}\ (\tilde{g} \to q\bar{q}\tilde{\chi}_1^0)$				
Requirement	Signal Region				
	RJR-C1	**RJR-C2**	**RJR-C3**	**RJR-C4**	**RJR-C5**
$R_{ISR} \geq$	0.95	0.9	0.8	0.7	0.7
p_{TS}^{CM} [GeV] $\geq$	1000	1000	800	700	700
$\Delta\phi_{ISR,\,I}/\pi \geq$	0.95	0.97	0.98	0.95	0.95
$\Delta\phi(\mathrm{jet}_{1,2}, \vec{E}_T^{miss})_{\min} >$	-	-	-	0.4	0.4
M_{TS} [GeV] $\geq$	–	100	200	450	450
$N_{jet}^V \geq$	1	1	2	2	3
$|\eta_{jV}| \leq$	2.8	1.2	1.4	1.4	1.4

Table 3: Selection criteria and targeted signal model from Fig. 1 used to define signal regions in the RJR-based search, indicated by the prefix 'RJR'. Each SR is labelled with the targeted SUSY particle or the targeted region of parameter space, such that 'S', 'G' and 'C' denote regions searching for squark-, gluino-pair production, or compressed spectra, respectively.

7.3 Meff-based and RJR-based signal region comparison

Even though the selection requirements which define the Meff-based and RJR-based SRs are based on different sets of kinematic observables, the regions are not necessarily orthogonal. The fraction of events in common between different regions, for both SM backgrounds and SUSY signals, is reflective of the complementarity of using these two approaches. For models with large $\tilde{q}/\tilde{g}$ masses, the signal efficiency

is prioritized due to low production cross-sections. In these cases, stringent requirements on the similarly behaving m_{eff} and $H_{\text{T }2,1}^{\text{PP}}/H_{\text{T }4,1}^{\text{PP}}$ variables result in a larger overlap between the Meff-based and RJR-based signal regions. Conversely, signal regions designed for increasingly compressed mass spectra have looser m_{eff} and $H_{\text{T }2,1}^{\text{PP}}/H_{\text{T }4,1}^{\text{PP}}$, and backgrounds must be suppressed with other, complementary, kinematic requirements. As these additional kinematic observables can be quite different between Meff-based and RJR-based approaches, the orthogonality of these respective SRs increases with decreasing sparticle mass-splittings.
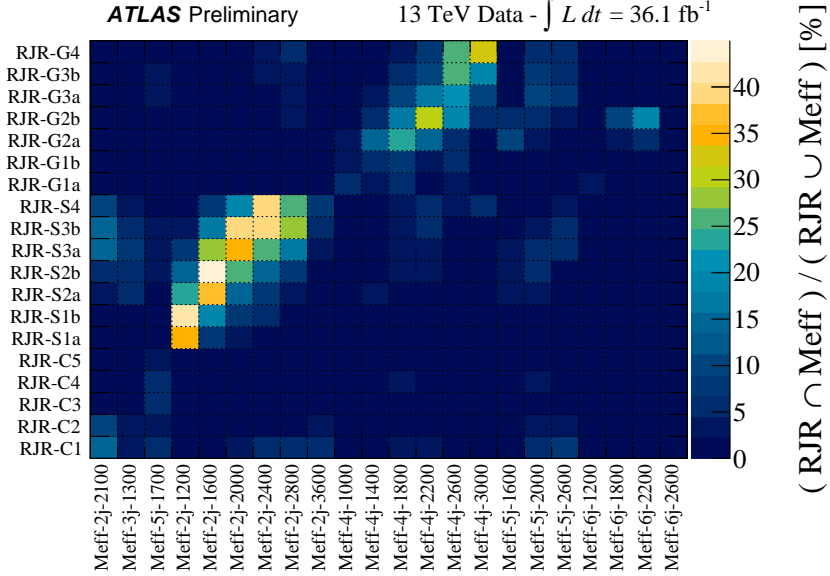
Figure 3: Fractional overlap of data events selected in Meff-based and RJR-based SRs. Meff-based SRs are listed along the x-axis with RJR-based regions on the y-axis. The intersection events falling in each pair of regions, normalized by the union, is shown on the z-axis. The Meff-based boosted boson SRs (Meff-2jB-1600,Meff-2jB-2400) are not included as they have negligible overlap with other regions due to their unique requirements.

This behavior can be observed in Figure 3 which shows the fractional overlap of selected events in data between the Meff-based and RJR-based SRs. Each of the axes listing the various SRs are organized in the same order, with SRs targeting compressed mass spectra in the lower left of the figure, followed by squark regions with increasing sparticle masses, and then gluinos. This ordering results in a diagonal pattern of larger overlap, as SRs targeting the same signals are more similar. The SRs searching for evidence of squark production (RJR-Sx and Meff-2j-x) have fractions of overlapping events between 25% and 45%, while those targeting gluino production (RJR-Gx and Meff-4j-x) have smaller intersections, ranging from a few to 30%. This decrease in overlap for gluino SRs follows from increasing differences between the selections used in the Meff-based and RJR-based approaches. While observables like $E_{\text{T}}^{\text{miss}}/m_{\text{eff}}(N_{\text{j}})$ and aplanarity are sensitive to global event properties, the RJR-based analysis for gluinos attempts to decompose the event into two hemispheres representing each gluino. Selection variables are calculated from each hemisphere independently, providing complementarity to those describing the total event. Using this additional information in the RJR-based selections leads to generally tighter SRs, adding increased sensitivity for intermediate mass-splittings.

Similar trends in event overlaps between SRs are expected for signal contributions, as shown in Fig. 4(a,b). Simulated (a) squark signal with $m_{\tilde{q}}$ = 1.5 TeV and massless $\tilde{\chi}_1^0$, and (b) gluino signal with $m_{\tilde{g}}$ = 2 TeV and massless $\tilde{\chi}_1^0$ are used as an example. In these cases, the squark and gluino-targeting SRs select a large fraction of the same events, with the RJR-S4 and Meff-2j-2800 regions best-suited to this squark signal

having 45% of selected events in common and the analogous gluino SRs (RJR-G4 and Meff-4j-3000) having an overlap of 40%. In case of squark signal, the largest overlap of 65% is seen with the RJR-S2a and Meff-2j-1600 with smaller overlap between tighter SRs favoured for this signal point.
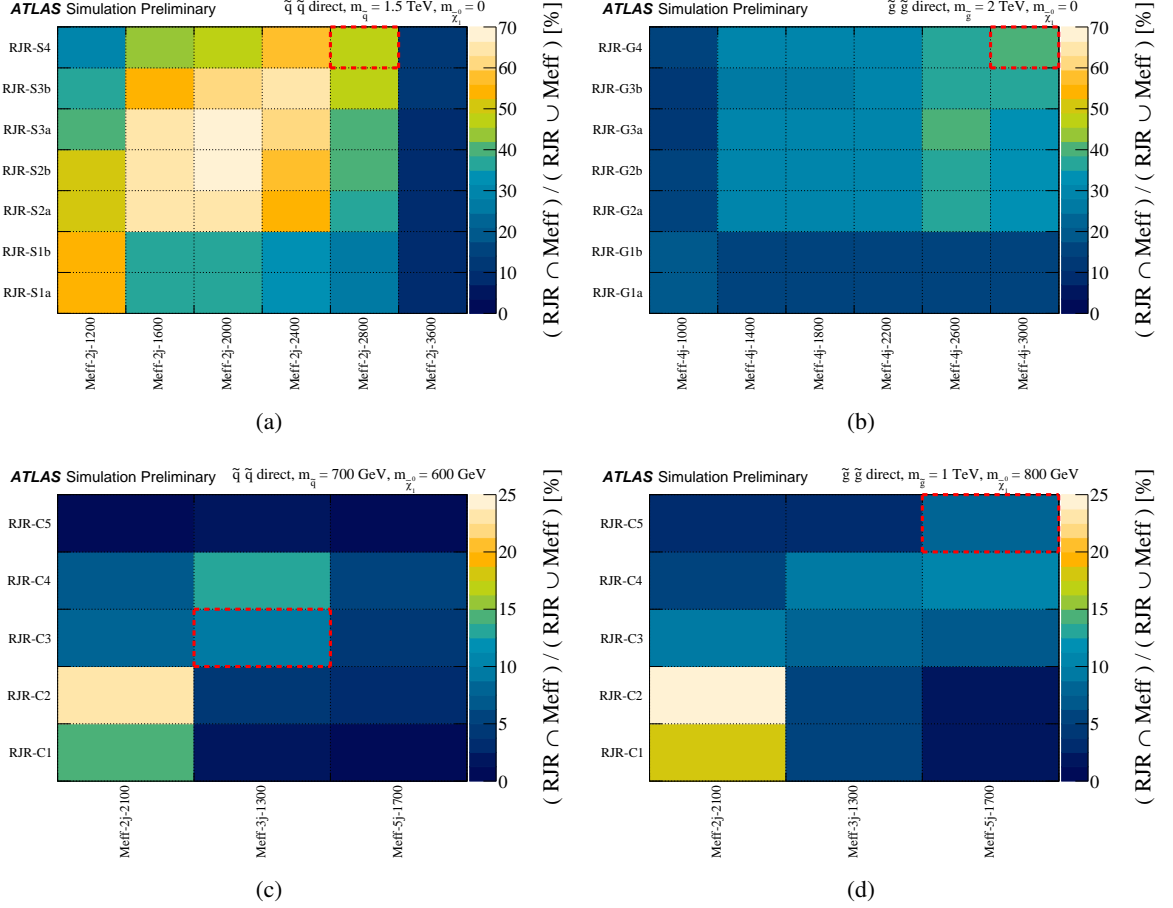

Figure 4: Fractional overlap of simulated squark and gluino pair events selected in Meff-based and RJR-based SRs. For these signals each squark (gluino) decays to one (two) quarks and a $\tilde{\chi}_1^0$. Figures correspond to simulated signals with (a) $m_{\tilde{q}} = 1.5$ TeV, $m_{\tilde{\chi}_1^0} = 0$, (b) $m_{\tilde{g}} = 2$ TeV, $m_{\tilde{\chi}_1^0} = 0$, (c) $m_{\tilde{q}} = 700$ GeV, $m_{\tilde{\chi}_1^0} = 600$ GeV, and (d) $m_{\tilde{g}} = 1$ TeV, $m_{\tilde{\chi}_1^0} = 800$ GeV. These selected signal points are near the limit of expected sensitivity for these SRs. Meff-based SRs are listed along the x-axis with RJR-based regions on the y-axis. The intersection events falling in each pair of regions, normalized by the union, is shown on the z-axis. The Meff and RJR-based SRs best suited to each signal, respectively, are indicated by dashed red boxes.

The RJR-Cx SRs targeting signals with the most compressed mass spectra ($0 < m_{\tilde{q}/\tilde{g}} - m_{\tilde{\chi}_1^0} \lesssim 200$ GeV) are the most dissimilar to their Meff-based analogues. They attempt to explicitly identify the strong initial-state radiation system which provides the escaping $\tilde{\chi}_1^0$'s the necessary E_T^{miss} for satisfying trigger and selection requirements and use kinematic requirements based on this interpretation of the event. The Meff-based SRs designed for these signals (Meff-2j-2100/3j-1300/5j-1700) exploit this compressed mass spectra event topology by requiring large $E_T^{\text{miss}}/\sqrt{H_T}$ and a hard leading jet corresponding to the ISR system, and the modest m_{eff} requirements result in SRs with relatively large expected background yields and low systematic uncertainties. The RJR-Cx SRs take a more restrictive approach, using observables designed specifically for this ISR event topology, with the corresponding SRs have much lower events yields, higher signal-to-background but larger uncertainties. This results in much smaller event overlap

for both signal and background, as seen in Fig. 4(c,d) for example simulated squark and gluino signals with $m_{\tilde{q}}$ = 700 GeV and $m_{\tilde{\chi}_1^0}$ = 600 GeV and $m_{\tilde{g}}$ = 1 TeV and $m_{\tilde{\chi}_1^0}$ = 800 GeV. For these signals, the overlap between the best-suited SRs (RJR-C3 and Meff-3j-1300 for the squark signal, RJR-C5 and Meff-5j-1700 for the gluino) is about only 10%. On the other hand, 65% (35%) of the signal events in RJR-C3 (RJR-C4) are also selected in Meff-3j-1300 (Meff-5j-1700). The more stringent selection strategy employed in the RJR-Cx regions leads to increased sensitivity for compressed mass-spectra for each of the signal variants considered in this analysis.

8 Background estimation

Standard Model background processes contribute to the event counts in the signal regions. The largest backgrounds in both searches presented here are: Z+jets, W+jets, top quark pairs, single top quarks, dibosons and multi-jet production. Non-collision backgrounds are negligible.

Generally the largest background, resulting from events with Z+jets, results from an irreducible component in which $Z \to \nu\bar{\nu}$ decays generate large E_T^{miss}. Similarly, most of the W+jets background is composed of $W \to \tau\nu$ events in which the τ-lepton decays to hadrons, with additional contributions from $W \to e\nu, \mu\nu$ events in which no baseline electron or muon is reconstructed, with E_T^{miss} following from produced neutrinos. Top quark pair production, followed by semileptonic decays, in particular $t\bar{t} \to b\bar{b}\tau\nu qq'$ (with the τ-lepton decaying to hadrons), as well as single-top-quark events, can also generate large E_T^{miss} and satisfy the jet and lepton-veto requirements. Each of these primary backgrounds are estimated using dedicated control regions, as described in the following section, while diboson production is estimated with MC simulated data normalized to NLO cross-section predictions, as described in Section 3.

The multi-jet background in the signal regions is due to missing transverse momentum from misreconstruction of jet energies in the calorimeters, jets misidentified as electrons, jets lost by JVT requirement, as well as neutrino production in semileptonic decays of heavy-flavour hadrons. After applying the requirements based on $\Delta\phi(\text{jet}, \vec{E}_T^{\text{miss}})_{\text{min}}$ and $E_T^{\text{miss}}/m_{\text{eff}}(N_j)$ in Meff-based search, or Δ_{QCD}, $p_T^{\text{PP}}/H_{T\,2,1}^{\text{PP}}$ and $\Delta\phi(\text{jet}, \vec{E}_T^{\text{miss}})_{\text{min}}$ in RJR-based search, as indicated in Tables 2 and 3, the remaining multi-jet background is negligible.

8.1 Control regions

In order to estimate the expected background yields, control regions are defined for each of the signal regions in four different final states. In the Meff-based search, each SR has its own set of four CRs, while in the RJR-based search, a common set of CRs is used for all SRs in every targeted signal category (RJR-S, RJR-G or RJR-C). The CR selections are optimized to maintain an adequate statistical precision while minimizing the systematic uncertainties arising from the extrapolation of the CR event yield to estimate the background in the SR. The latter is addressed through the fact that the same jet p_T thresholds and $m_{\text{eff}}(\text{incl.})$ selections in the CRs are used as for the SR in the Meff-based search. Similarly, in the RJR-based search requirements on discriminating variables are chosen to match those used in SRs as closely as possible. The basic CR definitions in both searches are listed in Table 4.

CR	SR background	CR process	CR selection (Meff-based)	CR selection (RJR-based)
Meff/RJR-CRγ	$Z(\to \nu\bar{\nu})$+jets	γ+jets	Isolated photon	Isolated photon
Meff/RJR-CRQ	Multi-jet	Multi-jet	SR with reversed requirements on (i) $\Delta\phi(\text{jet}, \vec{E}_T^{\text{miss}})_{\text{min}}$ and (ii) $E_T^{\text{miss}}/m_{\text{eff}}(N_j)$ or $E_T^{\text{miss}}/\sqrt{H_T}$	$\Delta_{\text{QCD}} < 0$ reversed requirement on $H_{1,1}^{\text{PP}}$ (RJR-S/G) or $R_{\text{ISR}} < 0.5$ (RJR-C)
Meff/RJR-CRW	$W(\to \ell\nu)$+jets	$W(\to \ell\nu)$+jets	30 GeV$< m_T(\ell, E_T^{\text{miss}}) < 100$ GeV, b-veto	
Meff/RJR-CRT	$t\bar{t}$(+EW) and single top	$t\bar{t} \to b\bar{b}qq'\ell\nu$	30 GeV$< m_T(\ell, E_T^{\text{miss}}) < 100$ GeV, b-tag	

Table 4: Summary of CRs for the Meff-based and RJR-based searches. Also listed are the main targeted background in the SR in each case, the process used to model the background, and the main CR requirement(s) used to select this process. The transverse momenta of high-purity leptons (photons) used to select CR events must exceed 27 (150) GeV. The jet p_T thresholds and m_{eff}(incl.) selections match those used in the corresponding SRs of Meff-based search. For the RJR-based search, selections are based on the discriminating variables used in the defining SRs, as described in the text.

The γ+jets region in both searches (labelled as Meff/RJR-CRγ in Table 4) is used to estimate the contribution of $Z(\to \nu\bar{\nu})$+jets background events to each SR by selecting a sample of γ+jets events with $p_T(\gamma) > 150$ GeV and then treating the reconstructed photon as invisible in the E_T^{miss} calculation. For $p_T(\gamma)$ significantly larger than m_Z the kinematic properties of such events strongly resemble those of Z+jets events [16]. In order to reduce the theoretical uncertainties associated with the Z/γ^*+jets background expectations in SRs arising from the use of LO γ+jets cross-sections, a correction factor is applied to the Meff/RJR-CRγ events as a function of the requirement on the number of jets. This correction factor, κ, ranges from 1.41 to 2.26 for two to six jets, and is determined by comparing Meff-CRγ observations with those in a highly populated auxiliary control region defined by selecting events with two electrons or muons for which the invariant mass lies within 25 GeV of the mass of the Z boson, satisfying $E_T^{\text{miss}} > 250$ GeV, $E_T^{\text{miss}}/\sqrt{H_T} > 14$ GeV$^{1/2}$ and m_{eff}(incl.) > 1200 GeV where two leptons are treated as contributing to E_T^{miss}.

The W and top regions in both searches (labelled as Meff/RJR-CRW and Meff/RJR-CRT in Table 4) aim to select samples rich in $W(\to \ell\nu)$+jets and semileptonic $t\bar{t}$ background events, respectively. They use events with one high-purity lepton with $p_T > 27$ GeV and differ in their number of b-jets (zero or ≥ 1, respectively). In both searches, the requirement on the transverse mass m_T formed by the E_T^{miss} and a selected lepton is applied, as indicated in Table 4. The lepton is treated as a jet with the same momentum to model background events in which a hadronically decaying τ-lepton is produced. The Meff-CRW and Meff-CRT selections omit the SR selection requirements on $|\eta_{\text{jet}}|$, $\Delta\phi(\text{jet}, \vec{E}_T^{\text{miss}})_{\text{min}}$ and aplanarity for all SRs, while for the SRs requiring m_{eff}(incl.) > 2200 GeV the requirements on $E_T^{\text{miss}}/m_{\text{eff}}(N_j)$ are not applied. This is done in order to increase the number of CR data events without significantly increasing the theoretical uncertainties associated with the CR-to-SR extrapolation in the background estimation procedure.

The multi-jet background in both searches is estimated using a data-driven technique [16], which applies a resolution function to well-measured multi-jet events in order to estimate the impact of jet energy mismeasurement and heavy-flavour semileptonic decays on E_T^{miss} and other variables. The resolution function of jets is initially estimated from MC simulation by matching 'truth' jets reconstructed from generator-level particles including muons and neutrinos to detector-level jets with $\Delta R < 0.1$ in multi-jet samples, and then is modified to agree with data in dedicated samples to measure the resolution fuction.

The Meff-CRQ region uses reversed selection requirements on $\Delta\phi(\text{jet}, \vec{E}_\text{T}^\text{miss})_\text{min}$ and on $E_\text{T}^\text{miss}/m_\text{eff}(N_\text{j})$ (or $E_\text{T}^\text{miss}/\sqrt{H_\text{T}}$ where appropriate) to produce samples enriched by multi-jet background events.

In the RJR-based search, all CRs corresponding to RJR-S (RJR-G) SRs are required to satisfy $H_{1,1}^\text{PP} > 800\ (700)$ GeV . Additionally, $H_{\text{T}\ 2,1}^\text{PP} > 1000$ GeV, $H_{\text{T}\ 4,1}^\text{PP} > 1200$ GeV and $M_\text{TS} > 0$ GeV are required for RJR-CRW, RJR-CRT and RJR-CRQ, corresponding to RJR-S, RJR-G and RJR-C signal regions, respectively. In RJR-CRW and RJR-CRT, the requirements on all the other variables used for the RJR-SR selections are chosen such that the loosest value in the SR category (RJR-S, RJR-G or RJR-C) indicated in Table 3 is chosen. No requirement on $p_{\text{PP},z}^\text{lab}/\left(p_{\text{PP},z}^\text{lab} + H_{\text{T}\ N,1}^\text{PP}\right)$ is used for the RJR-CRQ selections in all RJR-SRs, where $N = 2$ or 4.
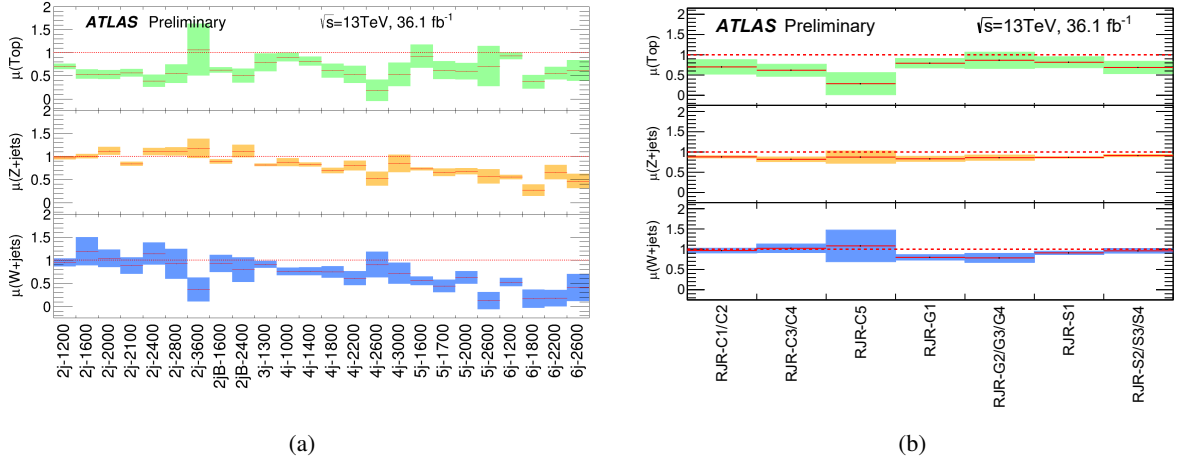

(a) (b)

Figure 5: Fitted normalization factor per process as a function of the channel considered in the (a) Meff-based and (b) RJR-based searches. The dashed horizontal lines at 1 correspond to pure Monte Carlo estimates.

The normalization factors determined in each CR for each background process are shown in Figure 5. Some trends in these factors are observed, with the normalization factors for top background becoming smaller with increasingly tight m_eff cuts for the Meff-based regions. Similarly, the measured top normalization factors decrease with increasingly tight M_TS and N_V requirements in the RJR-based search. This behavior follows from the simulated top MC samples exhibiting generally harder kinematics than observed in data, as seen in Figure 6(d) and 7(d). The normalization factors for W+jets and Z+jets processes are generally stable with changing kinematics cuts but with a clear indication that they become systematically smaller with increasingly strict requirements on the jet multiplicity. This is due to the MC simulation predicting higher event jet multiplicities relative to what is observed in data.

Example $m_\text{eff}(\text{incl.})$ distributions in control regions associated with Meff-4j-2200 selections are shown in Figure 6. Figure 7 shows the p_TS^CM discriminant variable distributions in control regions corresponding to RJR-C1 signal region selections. In all CRs, the data distributions are consistent with the MC background prediction within uncertainties after normalizing the dominant process in each CR.
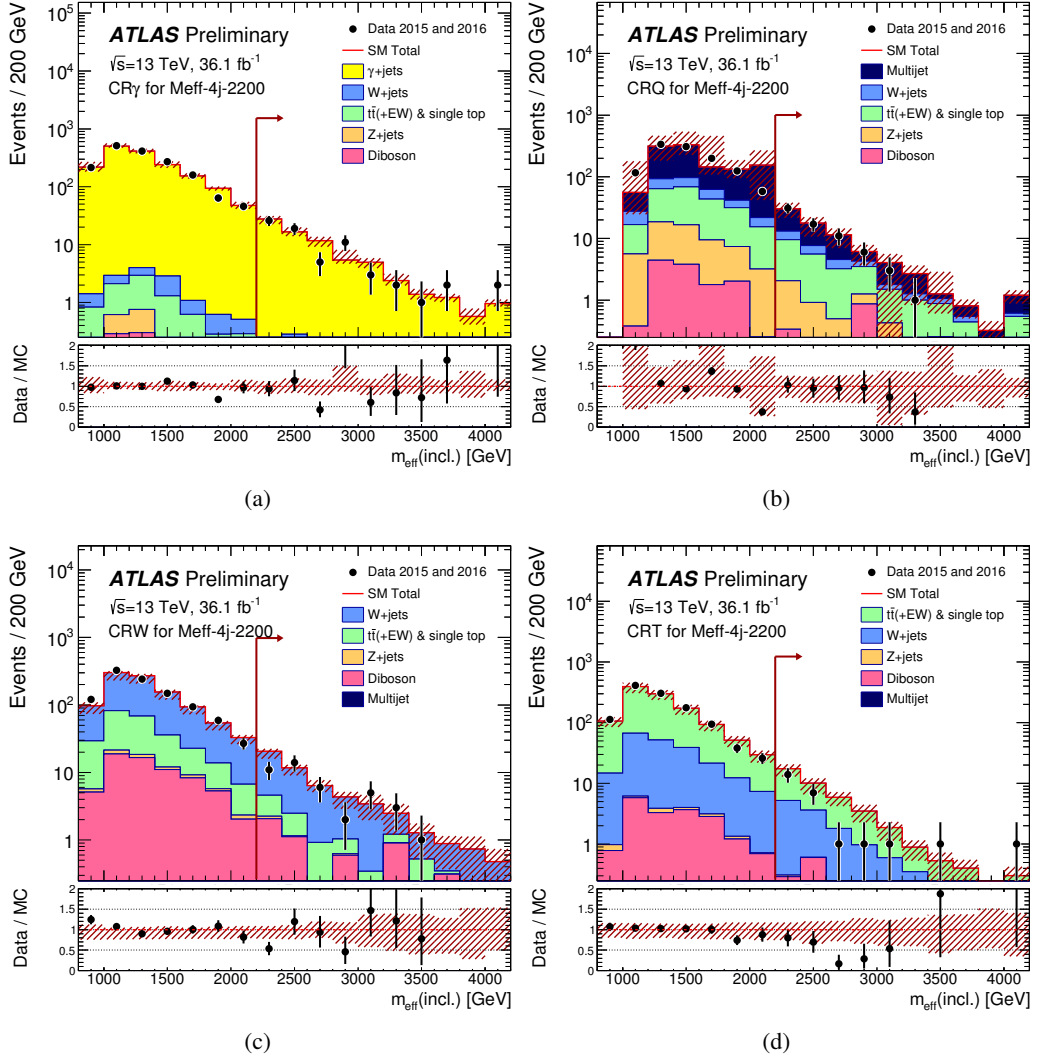
Figure 6: Observed m_{eff}(incl.) distributions in control regions (a) Meff-CRγ, (b) Meff-CRQ, (c) Meff-CRW and (d) Meff-CRT after selecting events with at least four energetic jets as indicated in Table 2 for Meff-4j-2200 after applying all selection requirements except those on the plotted variable. No selection requirements on $\Delta\phi(\mathrm{jet}, \vec{E}_{\mathrm{T}}^{\mathrm{miss}})_{\mathrm{min}}$ are applied in Meff-CRW and Meff-CRT regions. The arrows indicate the values at which the requirements on m_{eff}(incl.) are applied. The histograms denote the MC background expectations, normalized to cross-section times integrated luminosity and the dominant process in each CR is normalized to data. In case of γ+jets background, a κ factor described in the text is applied. The last bin includes the overflow. The hatched (red) error bands denote the combined experimental, MC statistical and theoretical modelling uncertainties.
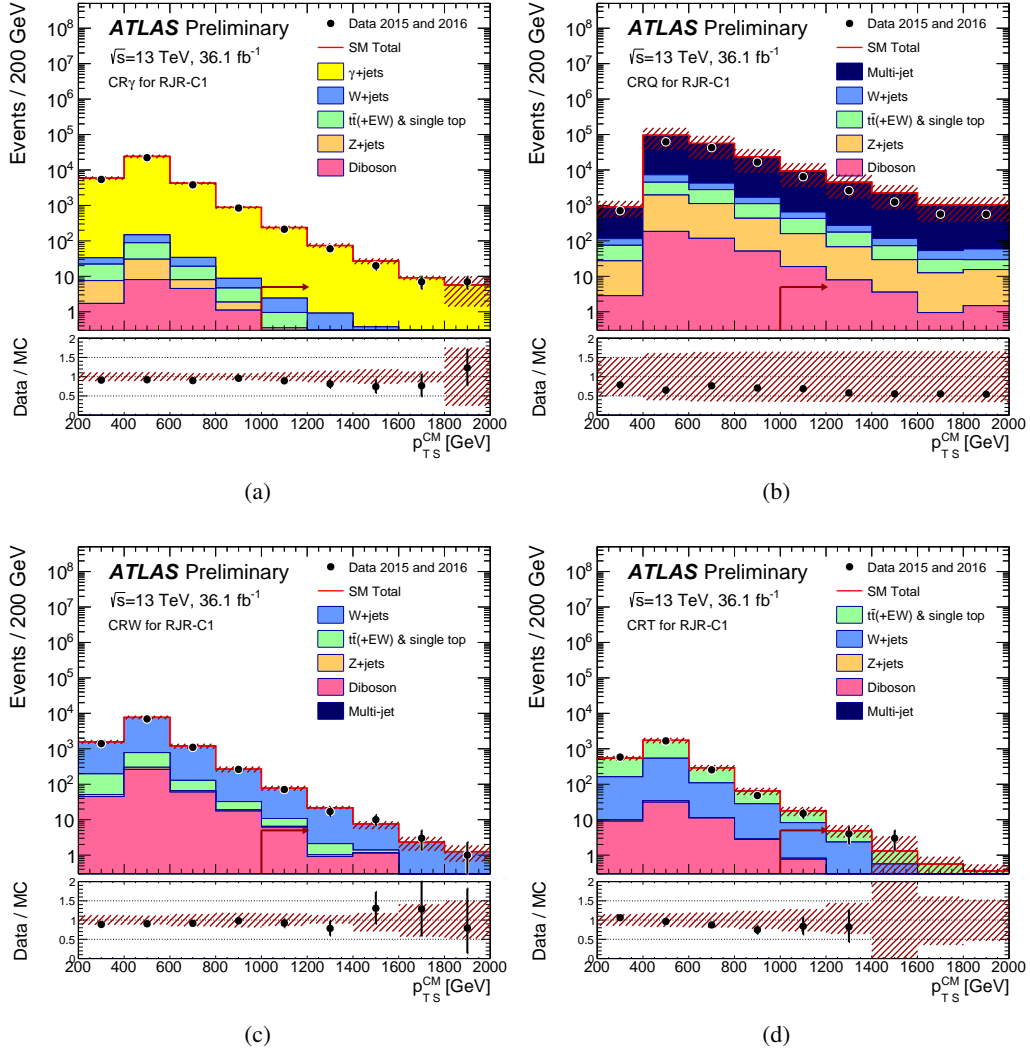
Figure 7: Observed $p_{\mathrm{TS}}^{\mathrm{CM}}$ distribution in control regions (a) RJR-CRγ, (b) RJR-CRQ, (c) RJR-CRW and (d) RJR-CRT after selecting events for the corresponding control regions as explained in the text for RJR-C1 region and after applying all selection requirements except those on the plotted variable. The arrows indicate the values at which the requirements are applied. The histograms denote the MC background expectations, normalized to cross-section times integrated luminosity and the dominant process in each CR is normalized to data. In case of γ+jets background, a κ factor described in the text is applied. The last bin includes the overflow. The hatched (red) error bands denote the combined experimental, MC statistical and theoretical modelling uncertainties.

8.2 Validation regions

The background estimation procedure is validated by comparing the numbers of events observed in the VRs to the corresponding SM background expectations obtained from the background-only fits. Several VRs are selected in both searches, with requirements distinct from those used in the CRs, which maintain low expected signal contamination.

24

The Meff/RJR-CRγ estimates of the $Z(\rightarrow \nu\bar{\nu})$+jets background are validated using samples of $Z(\rightarrow \ell\bar{\ell})$+jets events selected by requiring high-purity lepton pairs of opposite sign and identical flavour for which the dilepton invariant mass lies within 25 GeV of the Z boson mass (Meff/RJR-VRZ). In Meff/RJR-VRZ regions, the leptons are treated as contributing to $E_{\mathrm{T}}^{\mathrm{miss}}$. Additional VRs designed to validate the $Z(\rightarrow \ell\bar{\ell})$+jets estimation in the RJR-based search are also used: VRZc region, which selects events with no leptons but requires inverted selection based on $\Delta\phi_{\mathrm{ISR, I}}$ requirement compared to the SR selection (Table 3) and VRZca, which on top of VRZc selection additionally applies looser set of requirements on SR discriminant variables, as listed for the RJR-CRW and RJR-CRT regions. In order to increase the statistics in RJR-VRZ regions, two additional regions, RJR-VRZa and RJR-VRZb are constructed with additionally loosened $H_{1,1}^{\mathrm{PP}}$ and $H_{\mathrm{T}\,2,1}^{\mathrm{PP}}$ (or $H_{\mathrm{T}\,4,1}^{\mathrm{PP}}$ where appropriate) to the values used for the RJR-CRW and RJR-CRT regions.

The Meff-CRW and Meff-CRT estimates of the W+jets and top quark background are validated with the same Meff-CRW and Meff-CRT selections, but reinstating the requirement on $\Delta\phi(\mathrm{jet}, \vec{E}_{\mathrm{T}}^{\mathrm{miss}})_{\mathrm{min}}$ and treating the lepton as a jet (Meff-VRW, Meff-VRT). Similarly, the RJR-CRW and RJR-CRT estimates of the W+jets and top quark background are validated using the same selections as for the corresponding CRs, except that the requirements on $H_{1,1}^{\mathrm{PP}}$ and M_{TS} (RJR-VRWa, RJR-VRTa) or $H_{\mathrm{T}\,2,1}^{\mathrm{PP}}$ and $H_{\mathrm{T}\,4,1}^{\mathrm{PP}}$ (RJR-VRWb, RJR-VRTb) are omitted. Two additional VRs that require the presence of a high-purity lepton and either apply veto (RJR-VRW) or require the presence of at least one b-jet (RJR-VRT), and require no additional SR selection criteria, are also used in the analysis.

The Meff-CRQ estimates of the multi-jet background are validated with VRs for which the Meff-CRQ selection is applied, but with the SR $E_{\mathrm{T}}^{\mathrm{miss}}/m_{\mathrm{eff}}(N_{\mathrm{j}})$ ($E_{\mathrm{T}}^{\mathrm{miss}}/\sqrt{H_{\mathrm{T}}}$) requirement reinstated (Meff-VRQa), or with a requirement of an intermediate value of $\Delta\phi(\mathrm{jet}, \vec{E}_{\mathrm{T}}^{\mathrm{miss}})_{\mathrm{min}}$ applied (Meff-VRQb). For the RJR-VRQ region, the same selection as for the corresponding RJR-CRQ is used, except that the requirements on $H_{1,1}^{\mathrm{PP}}$, $H_{\mathrm{T}\,2,1}^{\mathrm{PP}}$ (or $H_{\mathrm{T}\,4,1}^{\mathrm{PP}}$ where appropriate) and M_{TS} are omitted depending on the region. Additional VRs with inverted Δ_{QCD} (RJR-VRQa), $H_{1,1}^{\mathrm{PP}}$ (RJR-VRQb) for RJR-S and RJR-G signal regions, and with 0.5 $< R_{\mathrm{ISR}} <$ SR requirement for RJR-C regions (Table 3), are also used.

The MC estimates of the diboson background are validated with VRs for the samples of $WZ(\rightarrow \ell\nu\ell\bar{\ell})$+jets events selected by requiring three high-purity leptons including a lepton pair of opposite sign and identical flavour for which the dilepton invariant mass lies within 25 GeV of the Z boson mass (Meff-VR3L). In these regions, the opposite sign and identifal flavour lepton pair are treated as contributing to $E_{\mathrm{T}}^{\mathrm{miss}}$ to emulate the dominant diboson background processes in SR such as $WZ(\rightarrow q\bar{q}'\nu\bar{\nu})$+jets and $WZ(\rightarrow l\nu\nu\bar{\nu})$+jets.
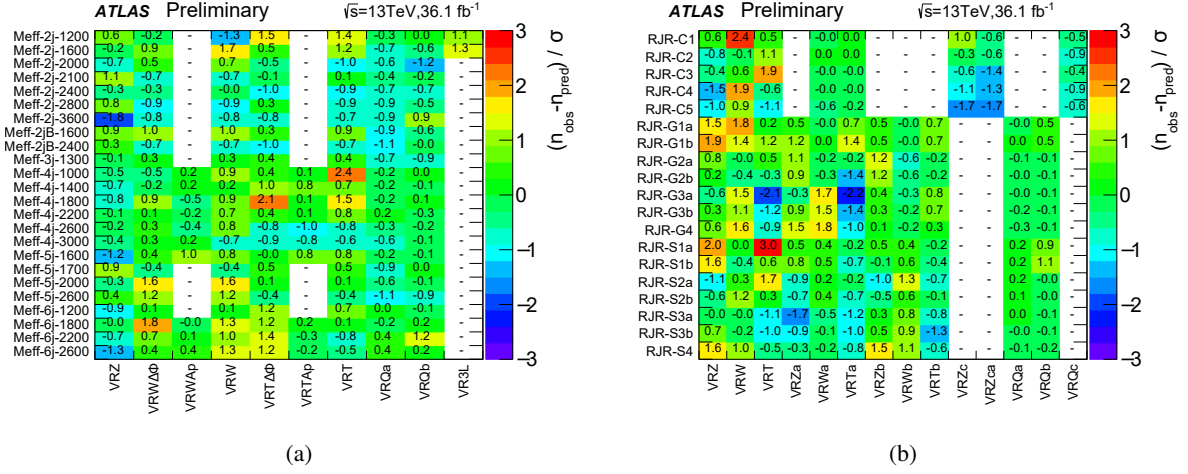
(a)

(b)

Figure 8: Differences between the numbers of observed events in data and the SM background predictions for each VR used in the (a) Meff-based and (b) RJR-based searches, expressed as a fraction of the total uncertainty which combines the uncertainty on the background expectations, and the expected statistical uncertainty of the test obtained from the number of expected events. Empty boxes (indicated by a '-') are when VR is not used for the corresponding SR selection.

The results of the validation procedure are shown in Figure 8, where the difference in each VR between the numbers of observed and expected events, expressed as fractions of the one-standard deviation (1σ) uncertainties on the latter, are summarized. Most VR observations lie within 1σ of the background expectations for both searches, with the largest discrepancy being 2.4σ in the Meff-VRT associated with the SR Meff-4j-1000 out of 190 VRs and 2.8σ in RJR-VRT associated with the SR RJR-S1a out of 194 VRs.

9 Systematic uncertainties

Systematic uncertainties in background estimates arise from the use of extrapolation factors which relate observations in the control regions to background expectations in the signal regions, and from the MC modelling of minor backgrounds.

The overall background uncertainties, detailed in Figure 9, range from 6% in SR Meff-2j-1200 to 67% in SR Meff-6j-2600 and from 10% in SRs RJR-S1a, RJR-S2a, RJR-G1a, RJR-C2 and RJR-C3 to 24% in SR RJR-SRG3b.

For the backgrounds estimated with MC simulation-derived extrapolation factors, the primary common sources of systematic uncertainty are the jet energy scale (JES) calibration, jet energy resolution (JER), theoretical uncertainties, and limited event yields in the MC samples and data CRs. Correlations between uncertainties (for instance between JES or JER uncertainties in CRs and SRs) are taken into account where appropriate.

The JES uncertainty was measured using the techniques described in Refs. [85, 99, 100]. The JER uncertainty is estimated using the methods discussed in Refs. [85, 101]. An additional uncertainty in the

modelling of energy not associated with reconstructed objects, used in the calculation of $E_{\mathrm{T}}^{\mathrm{miss}}$ and measured with unassociated charged tracks, is also included. The combined JES, JER and $E_{\mathrm{T}}^{\mathrm{miss}}$ uncertainty ranges from 1% of the expected background in 2-jet Meff-SRs to 14% in SR Meff-6j-2600. In the RJR-based search, the same uncertainties range from 1% in RJR-C4 to 12% in RJR-SRC5. Uncertainties on jet mass scale (JMS) and jet mass resolution (JMR) are additionally assigned to SR Meff-2jB-1600 and Meff-2jB-2400 which have requirements on the masses of large-radius jets. The JMS uncertainty is evaludated as the same methodology as Ref. [102]. For JMR uncertainty, 20% is assigned conservatively on the JMR. Combined JMS and JMR uncertainty is 3.2% of the expected background in Meff-2j-1600 and 5.1% in Meff-2j-2400.

Uncertainties arising from theoretical modelling of background processes are evaluated by comparing samples produced with different MC generators or by varying scale uncertainties. Uncertainties in the W/Z+jets production are estimated by increasing and decreasing the renormalization, factorization and resummation scales a factor of two, and by increasing and decreasing the nominal CKKW matching scale, 20 GeV, by 10 GeV and 5 GeV, respectively. Uncertainties in the modelling of top quark pair production are estimated by comparing samples generated with Powheg-Box and MG5_aMC@NLO, and comparing the nominal sample with sample generated using different shower tunes. Uncertainties associated with PDF modelling of top quark pair production are found to be negligible. Uncertainties in diboson production due to PDF, renormalization and factorization scale uncertainties (estimated by increasing and decreasing the scales used in the MC generators by a factor of two for all combinations and taking envelop of them) are accounted. The combined uncertainty ranges from 3% in Meff-2j-1200 to 48% in Meff-6j-2600 for Meff SRs. In RJR-based search, the same uncertainties range from 8% in RJR-S1a to 18% in RJR-SRG4, with the smaller range largely due to the absence of six jet SRs. Uncertainties associated with the modelling of Z+jets production are largest in the 2-jet Meff-SRs (7%). In the RJR-based search, these uncertainties are maximal in RJR-SRS2b and RJR-SRS3b SR (8%). The impact of lepton reconstruction uncertainties, and of the uncertainties related to the b-tag/b-veto efficiency, on the overall background uncertainty are found to be negligible for all SRs.

The uncertainties arising from the data-driven correction procedure applied to events selected in the CRγ region, described in Section 8, are included in Figure 9 under 'CR statistical uncertainty'. Uncertainties related to the multi-jet background estimates are accounted for by applying a uniform 100% uncertainty of multi-jet yield in all SRs. In most of the SRs these uncertainties are negligible, and the maximum resulting contribution to the overall background uncertainty is less than 1%. Other uncertainties due to CR data statistics are combined to be from 4% to 32% for Meff SRs and from 4% to 20% for RJR SRs. The statistical uncertainty arising from the use of MC samples is largest in SRs Meff-6j-2600 (11%) and RJR-SRG4 (10%).
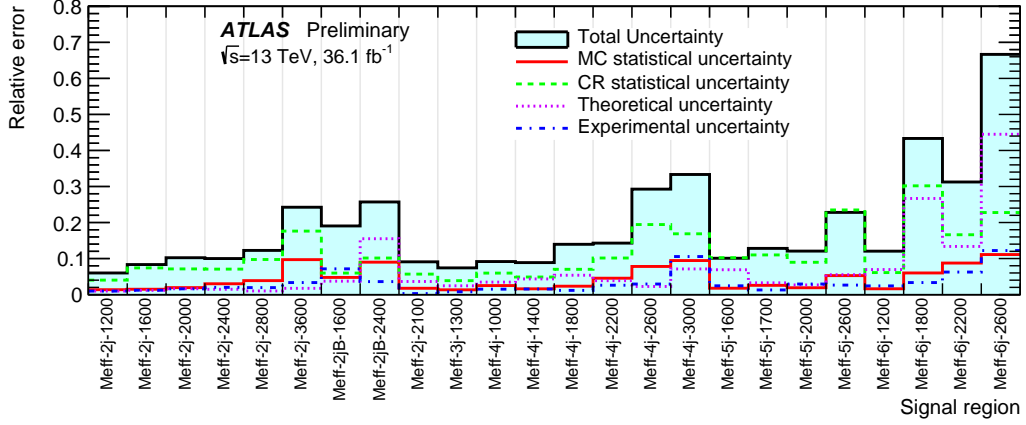
(a)
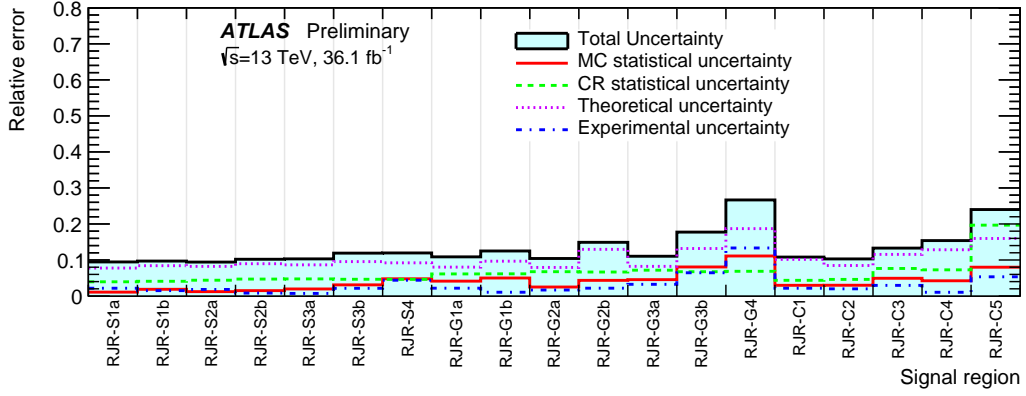
(b)

Figure 9: Breakdown of the largest systematic uncertainties in the background estimates for the (a) Meff-based and (b) RJR-based searches. The individual uncertainties can be correlated, such that the total background uncertainty is not necessarily their sum in quadrature.

Experimental uncertainties (JES, JER, JMS, JMR and $E_{\mathrm{T}}^{\mathrm{miss}}$) and MC statistical uncertainty on the SUSY signals are evaluated in the same way as the background and they are less than a few % for most of the signals in the targeted signal regions, except that 7% is assigned as JMS and JMR uncertainties in Meff-2jB-1600 and Meff-2jB-2400. The signal cross-section uncertainty is evaluated by computing the changes when the renormalization and factorization scale, PDF and the strong coupling constant (α_s) are varied. The uncertainties on the ISR and FSR on the SUSY signals are evaluated by varying generator tunes in the simulation as well as scales used in the matrix element generator as a function of the mass difference between gluino (or squark) and $\tilde{\chi}_1^0$, Δm. This uncertainty reaches 20% in the limit of no mass difference and is negligible for $\Delta m > 200$ GeV.

10 Results, interpretation and limits

Distributions of m_{eff}(incl.) from the Meff-based search for selected signal regions, obtained before the final selections on this quantity (but after applying all other selections), for data and the different MC samples normalized with the theoretical cross-sections, i.e. before applying the normalization from the CR fit, are shown in Figure 10. Similarly, distributions of the final discriminant variables used in the RJR-based search, $H_{\text{T 2,1}}^{\text{PP}}$ ($H_{\text{T 4,1}}^{\text{PP}}$ where appropriate) in selected RJR-S and RJR-G regions, and $p_{\text{TS}}^{\text{CM}}$ in selected RJR-C regions, after applying all other selection requirements except those based on the plotted variable, before applying the normalization from the CR fit, are shown in Figure 11. Examples of typical expected SUSY signals are shown for illustration. These signals correspond to the processes to which each SR is primarily sensitive: $\tilde{q}\tilde{q}$ production for the lower jet-multiplicity SRs and $\tilde{g}\tilde{g}$ production for the higher jet-multiplicity SRs. In these figures, data and background distributions largely agree within uncertainties.

The number of events observed in the data and the number of SM events expected to enter each of the signal regions, determined using the background-only fit, are shown in Tables 5 and 6 and in Figure 12. The pre-fit background expectations are also shown in Tables 5 and 6 for comparison.

The fit to the CRs for each SR compensates for the differences related to the overall normalization of the background seen in Figures 10 and 11, leading to good agreement between data and post-fit expectations in most of the SRs. The most significant observed excess across the signal regions for the Meff-based search, with a p-value for the background-only hypothesis of 0.02, corresponding to a significance of 2.14 standard deviations, occurs in SR Meff-2j-2100 (Table 5). The most significant observed excess across the signal regions for RJR-based search, with a p-value for the background-only hypothesis of 0.01, corresponding to a significance of 2.22 standard deviations, occurs in SR RJR-S1a (Table 6).
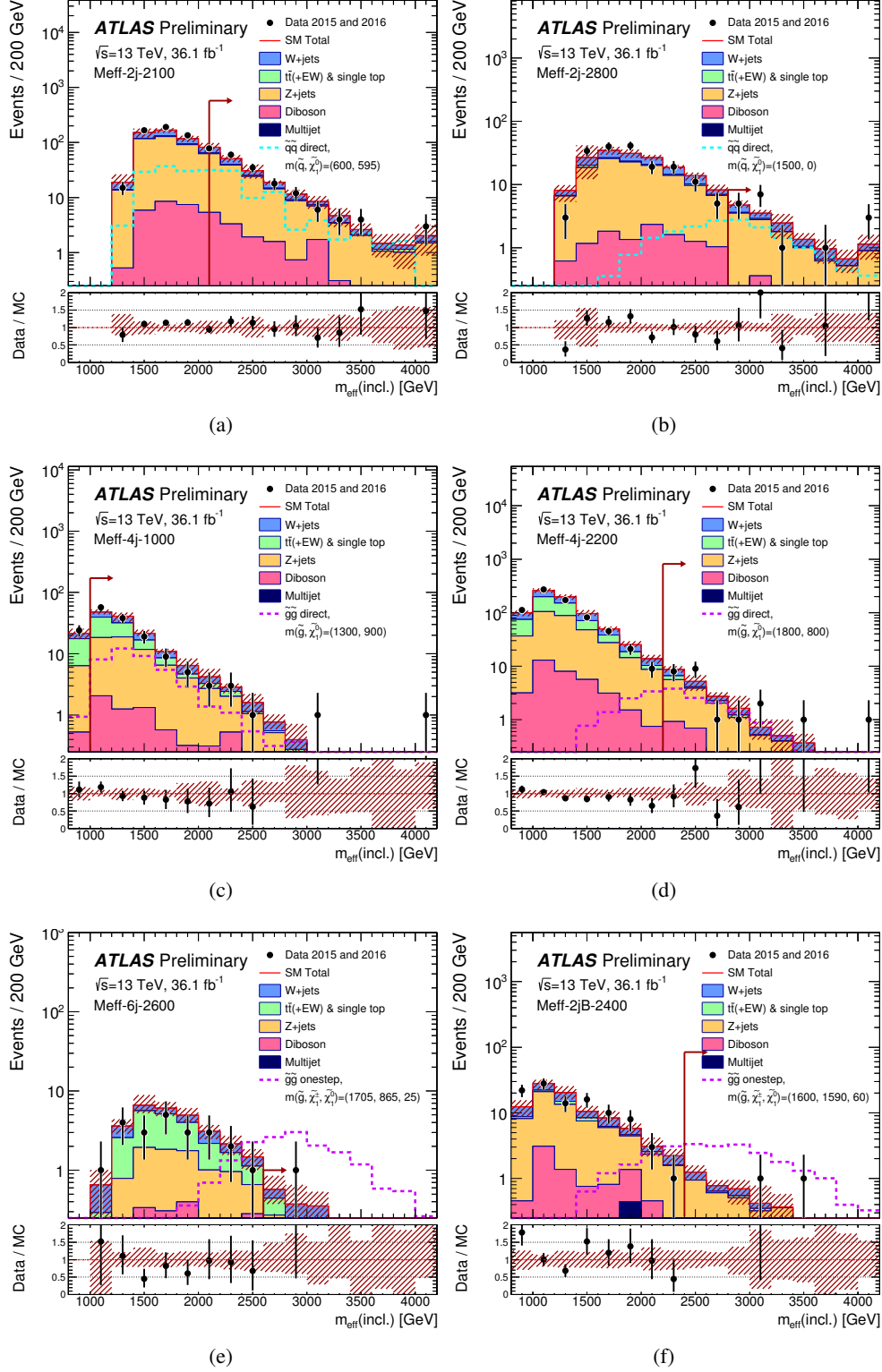
Figure 10: Observed m_{eff}(incl.) distributions for the (a) Meff-2j-2100, (b) Meff-2j-2800, (c) Meff-4j-1000, (d) Meff-4j-2200, (e) Meff-6j-2600 and (f) Meff-2jB-2400 signal regions, after applying all selection requirements except those on the plotted variable. The histograms denote the MC background expectations prior to the fits described in the text, normalized to cross-section times integrated luminosity. The last bin includes the overflow. The hatched (red) error bands denote the combined experimental and MC statistical uncertainties. The arrows indicate the values at which the requirements on m_{eff}(incl.) are applied. Expected distributions for benchmark signal model points, normalized to NLO+NLL cross-section (Section 3) times integrated luminosity, are also shown for comparison (masses in GeV).
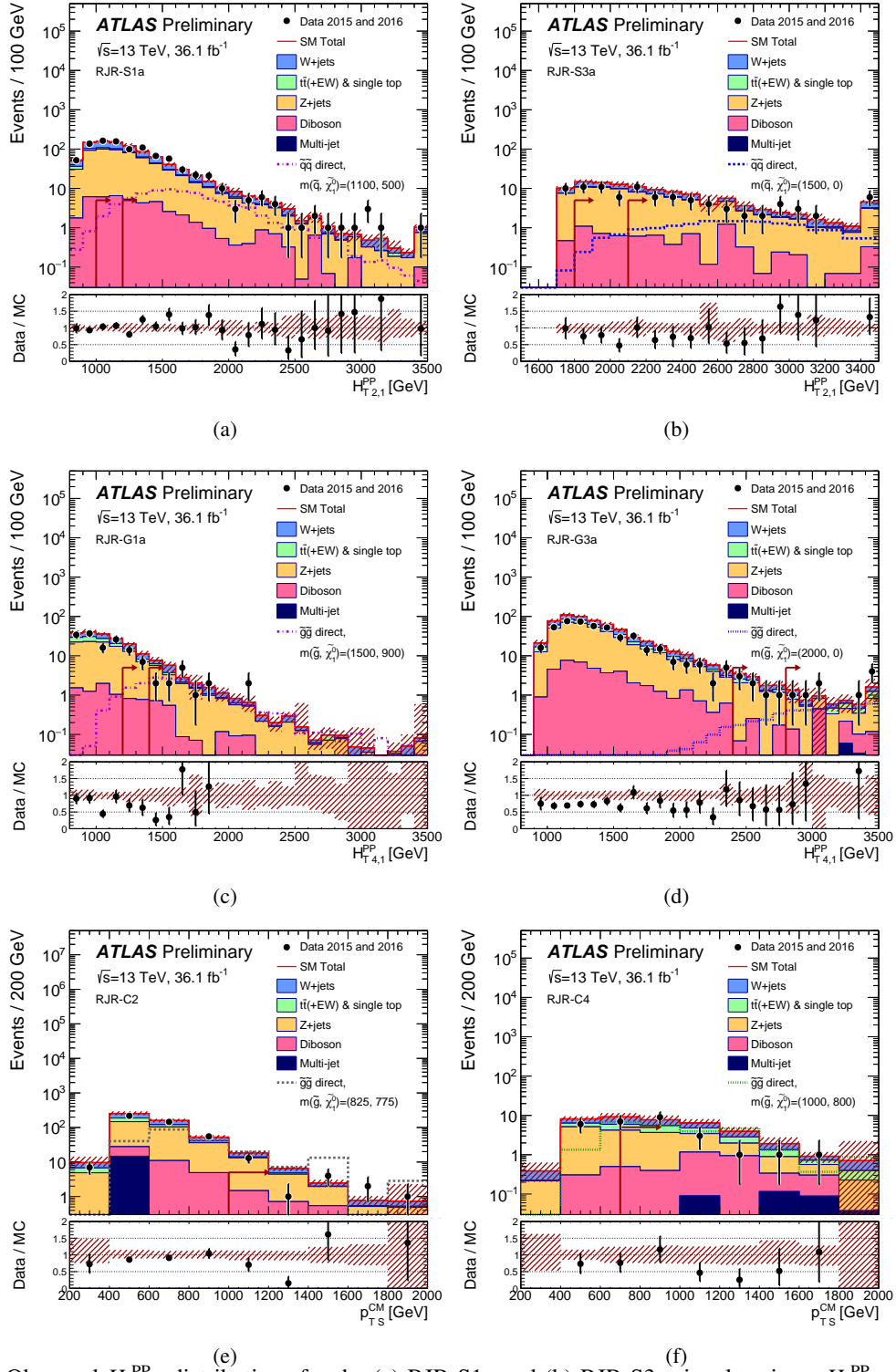
30

Figure 11: Observed $H_{\mathrm{T}\,2,1}^{\mathrm{PP}}$ distributions for the (a) RJR-S1a and (b) RJR-S3a signal regions, $H_{\mathrm{T}\,4,1}^{\mathrm{PP}}$ distributions for the (c) RJR-G1 and (d) RJR-G3 signal regions, and $p_{\mathrm{TS}}^{\mathrm{CM}}$ distributions for the (e) RJR-C2 and (f) RJR-C4 signal regions, after applying all selection requirements except those on the plotted variable. The histograms denote the MC background expectations prior to the fits described in the text, normalized to cross-section times integrated luminosity. The last bin includes the overflow. The hatched (red) error bands denote the combined experimental and MC statistical uncertainties. The arrows indicate the values at which the requirements on the plotted variable are applied. When two arrows are shown, these correspond to the looser SR variation 'a' and the tighter variation 'b'. Expected distributions for benchmark signal model points, normalized to NLO+NLL cross-section (Section 3) times integrated luminosity, are also shown for comparison (masses in GeV).

31
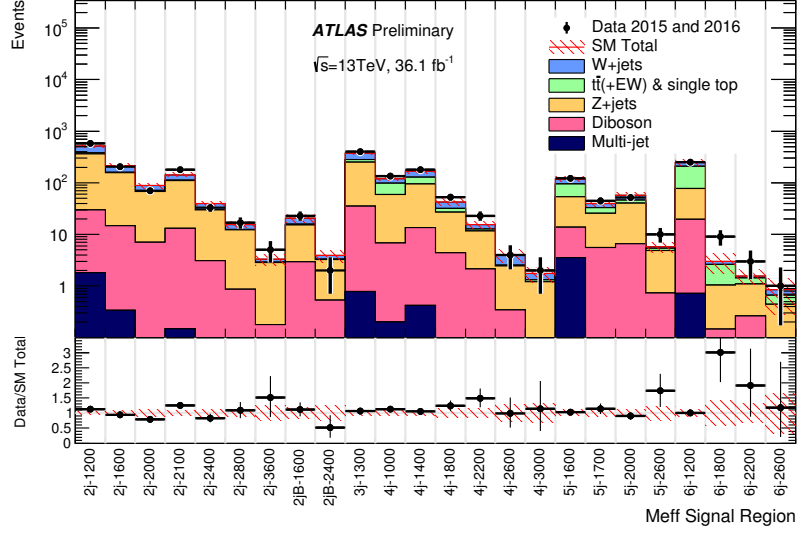
(a)
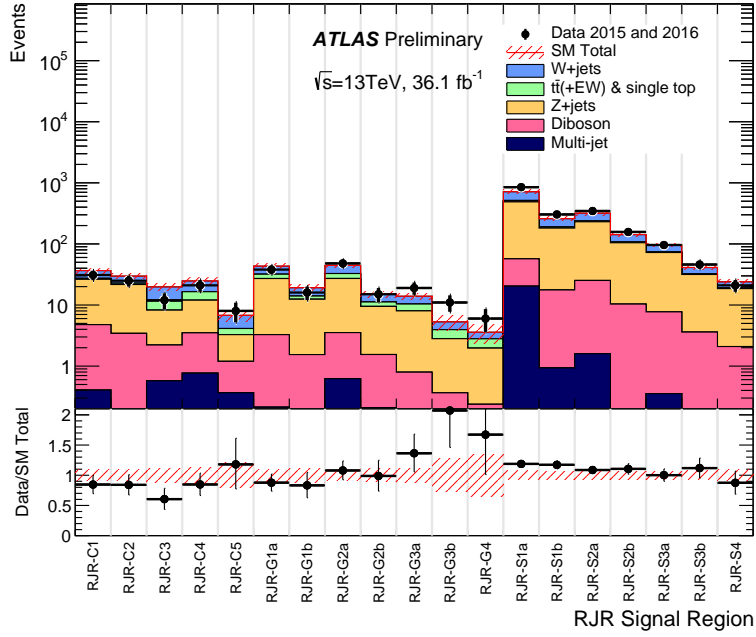
(b)

Figure 12: Comparison of the observed and expected event yields as a function of signal region in the (a) Meff-based and (b) RJR-based searches. The background expectations are those obtained from the background-only fits, presented in Tables 5 and 6.

In the absence of a statistically significant excess, limits are set on contributions to the SRs from BSM physics. Upper limits at 95% CL on the number of BSM signal events in each SR and the corresponding visible BSM cross-section are derived from the model-independent fits described in Section 5 using the CL_s prescription. Limits are evaluated using MC pseudo-experiments. The results are presented in

Signal Region [**Meff-**]	2j-1200	2j-1600	2j-2000	2j-2400	2j-2800	2j-3600	2j-B1600	2j-B2400
MC expected events								
Diboson	28.17	14.37	7.02	3.09	0.86	0.18	2.94	0.53
Z/γ^*+jets	346.37	140.61	54.13	24.23	10.22	2.28	13.84	2.45
W+jets	142.39	47.49	18.33	8.23	3.37	1.11	5.16	0.71
$t\bar{t}$(+EW) + single top	21.40	5.84	2.54	1.13	0.32	0.04	0.86	0.10
Fitted background events								
Diboson	28 ± 4	14.4 ± 2.3	7.0 ± 1.1	3.1 ± 0.5	0.86 ± 0.17	0.18 ± 0.07	2.9 ± 0.7	0.53 ± 0.1
Z/γ^*+jets	337 ± 19	141 ± 10	61 ± 8	26.8 ± 3.1	11.4 ± 1.4	2.7 ± 0.7	12.3 ± 1.8	2.7 ± 0.5
W+jets	136 ± 24	57 ± 16	19 ± 5	9.4 ± 2.6	3.1 ± 1.1	0.4 ± 0.31	4.8 ± 2.8	0.6 ± 0.6
$t\bar{t}$(+EW) + single top	15 ± 4	3.1 ± 1.7	1.34 ± 1.0	0.4 ± 0.4	0.18 ± 0.15	0.04 ± 0.04	0.5 ± 0.5	$0.05^{+0.57}_{-0.05}$
Multi-jet	1.8 ± 1.8	0.34 ± 0.34	–	–	–	–	–	–
Total bkg	517 ± 31	216 ± 18	88 ± 9	40 ± 4	15.5 ± 1.9	3.3 ± 0.8	21 ± 4	3.9 ± 1.0
Observed	582	204	70	33	17	5	23	2
$\langle\epsilon\sigma\rangle^{95}_{obs}$ [fb]	3.6	1.00	0.42	0.30	0.32	0.20	0.42	0.11
S^{95}_{obs}	131	36	15	11	11	7.1	15.1	4.1
S^{95}_{exp}	78^{+33}_{-21}	43^{+17}_{-12}	24^{+10}_{-6}	15^{+7}_{-4}	10^{+4}_{-3}	$5.4^{+2.0}_{-1.5}$	13^{+5}_{-3}	$5.0^{+2.3}_{-1.1}$
p_0 (Z)	0.06 (1.53)	0.50 (0.00)	0.50 (0.00)	0.50 (0.00)	0.33 (0.43)	0.19 (0.87)	0.37 (0.34)	0.50 (0.00)

Signal Region [**Meff-**]	2j-2100	3j-1300	4j-1000	4j-1400	4j-1800	4j-2200	4j-2600	4j-3000
MC expected events								
Diboson	12.87	34.43	6.56	13.18	4.40	2.14	0.35	0.06
Z/γ^*+jets	115.70	265.30	59.58	99.18	32.76	11.95	4.05	1.34
W+jets	33.90	105.92	28.91	51.75	14.57	4.49	1.66	0.61
$t\bar{t}$(+EW) + single top	4.96	36.08	42.86	41.67	7.64	1.71	0.63	0.21
Fitted background events								
Diboson	13 ± 5	34 ± 6	6.6 ± 1.2	13.2 ± 2.2	4.4 ± 0.9	2.1 ± 0.5	0.35 ± 0.08	0.06 ± 0.03
Z/γ^*+jets	97 ± 8	218 ± 20	52 ± 7	82 ± 9	23 ± 4	9.6 ± 1.9	2.1 ± 0.7	1.1 ± 0.5
W+jets	30 ± 9	96 ± 18	22 ± 7	39 ± 9	11 ± 5	2.74 ± 1.0	1.5 ± 0.9	0.43 ± 0.33
$t\bar{t}$(+EW) + single top	2.8 ± 1.6	28 ± 10	39 ± 7	33 ± 10	4.7 ± 3.2	0.9 ± 0.5	$0.12^{+0.15}_{-0.12}$	0.11 ± 0.1
Multi-jet	0.15 ± 0.15	$0.79^{+0.80}_{-0.79}$	0.20 ± 0.20	0.4 ± 0.4	–	–	–	–
Total bkg	143 ± 13	378 ± 28	120 ± 11	169 ± 15	43 ± 6	15.4 ± 2.2	4.0 ± 1.2	1.8 ± 0.6
Observed	180	405	135	179	53	23	4	2
$\langle\epsilon\sigma\rangle^{95}_{obs}$ [fb]	2.0	2.5	1.3	1.5	0.85	0.47	0.17	0.12
S^{95}_{obs}	70	91	47	55	31	17	6.1	4.4
S^{95}_{exp}	37^{+14}_{-9}	69^{+27}_{-17}	36 ± 10	40^{+16}_{-9}	21^{+8}_{-5}	10^{+5}_{-3}	$6.0^{+2.0}_{-1.8}$	$4.3^{+1.7}_{-1.0}$
p_0 (Z)	0.02 (2.14)	0.20 (0.85)	0.13 (1.13)	0.11 (1.24)	0.07 (1.45)	0.07 (1.45)	0.50 (0.00)	0.44 (0.14)

Signal Region [**Meff-**]	5j-1600	5j-1700	5j-2000	5j-2600	6j-1200	6j-1800	6j-2200	6j-2600
MC expected events								
Diboson	10.29	5.61	6.59	0.73	19.00	0.15	0.26	0.09
Z/γ^*+jets	55.12	30.42	49.38	7.32	103.92	3.29	1.26	0.76
W+jets	41.39	15.21	18.42	2.60	78.02	2.15	0.70	0.47
$t\bar{t}$(+EW) + single top	44.63	11.71	9.77	0.75	139.99	4.31	0.61	0.36
Fitted background events								
Diboson	10.3 ± 1.8	5.61 ± 1.0	6.6 ± 1.2	0.73 ± 0.13	19.0 ± 3.2	0.15 ± 0.11	0.26 ± 0.07	$0.09^{+0.11}_{-0.09}$
Z/γ^*+jets	40 ± 5	20 ± 4	34 ± 6	4.2 ± 1.3	58 ± 10	0.9 ± 0.5	0.8 ± 0.4	0.35 ± 0.22
W+jets	23 ± 7	6.7 ± 2.4	11.6 ± 3.1	$0.32^{+0.41}_{-0.32}$	41 ± 20	$0.36^{+0.59}_{-0.36}$	$0.12^{+0.18}_{-0.12}$	$0.19^{+0.27}_{-0.19}$
$t\bar{t}$(+EW) + single top	42 ± 11	7.2 ± 2.5	5.9 ± 2.3	0.5 ± 0.5	130 ± 23	1.6 ± 1.2	0.35 ± 0.24	$0.22^{+0.39}_{-0.22}$
Multi-jet	4 ± 4	–	–	–	0.72 ± 0.72	–	–	–
Total bkg	119 ± 12	39 ± 5	58 ± 7	5.7 ± 1.3	249 ± 30	3.0 ± 1.3	1.6 ± 0.5	0.8 ± 0.6
Observed	122	45	52	10	250	9	3	1
$\langle\epsilon\sigma\rangle^{95}_{obs}$ [fb]	1.03	0.60	0.48	0.30	2.1	0.35	0.16	0.11
S^{95}_{obs}	37	22	17	10.7	74	13	5.6	4.1
S^{95}_{exp}	35^{+12}_{-11}	17^{+7}_{-5}	20^{+8}_{-5}	$7.1^{+2.9}_{-2.1}$	61^{+23}_{-14}	$8.7^{+2.8}_{-1.8}$	$4.2^{+1.5}_{-0.6}$	$3.5^{+1.5}_{-0.2}$
p_0 (Z)	0.35 (0.37)	0.22 (0.78)	0.50 (0.00)	0.10 (1.25)	0.50 (0.00)	0.08 (1.43)	0.16 (1.00)	0.19 (0.89)

Table 5: Numbers of events observed in the signal regions used in the Meff-based analysis compared with background expectations obtained from the fits described in the text using pp collision data at $\sqrt{s} = 13$ TeV corresponding to an integrated luminosity of 36.1 fb^{-1}. Empty cells (indicated by a '-') correspond to estimates lower than 0.01. The p-values (p_0) give the probabilities of the observations being consistent with the estimated backgrounds. For an observed number of events lower than expected, the p-value is truncated at 0.5. Between parentheses, p-values are also given as the number of equivalent Gaussian standard deviations (Z). Also shown are 95% CL upper limits on the visible cross-section ($\langle\epsilon\sigma\rangle^{95}_{obs}$), the visible number of signal events (S^{95}_{obs}) and the number of signal events (S^{95}_{exp}) given the expected number of background events (and $\pm1\sigma$ excursions of the expectation).

Signal Region	RJR-S1a	RJR-S1b	RJR-S2a	RJR-S2b	RJR-S3a	RJR-S3b	RJR-S4
MC expected events							
Diboson	36.66	16.69	23.63	10.18	7.37	3.60	2.09
Z/γ^*+jets	496.41	189.08	222.22	101.96	69.97	30.32	17.83
W+jets	221.22	76.78	84.09	36.03	22.66	9.13	5.22
$t\bar{t}$(+EW) + single top	32.38	9.37	11.01	4.58	2.60	1.13	0.67
Fitted background events							
Diboson	37 ± 8	17 ± 4	24 ± 5	10.2 ± 2.6	7.4 ± 1.5	3.6 ± 1.3	2.1 ± 0.5
Z/γ^*+jets	430 ± 40	164 ± 14	205 ± 16	94 ± 8	65 ± 5	28.0 ± 2.3	16.5 ± 1.4
W+jets	201 ± 25	70 ± 9	80 ± 12	34 ± 5	21.6 ± 2.9	8.7 ± 1.3	5.0 ± 0.9
$t\bar{t}$(+EW) + single top	27 ± 6	7.7 ± 2.5	7.7 ± 3.4	3.2 ± 1.2	1.8 ± 0.6	0.79 ± 0.31	$0.47^{+0.53}_{-0.47}$
Multi-jet	20 ± 20	0.9 ± 0.9	1.6 ± 1.6	0.18 ± 0.18	0.36 ± 0.35	–	–
Total bkg	720 ± 50	259 ± 17	318 ± 21	142 ± 10	96 ± 6	41.1 ± 3.1	24.0 ± 2.1
Observed	850	304	346	157	96	46	21
$\langle\epsilon\sigma\rangle^{95}_{\mathrm{obs}}$ [fb]	6.12	2.36	1.66	1.16	0.67	0.54	0.27
S^{95}_{obs}	220	85.3	60.0	41.9	24.2	19.6	9.9
S^{95}_{exp}	121^{+46}_{-33}	$48.8^{+19.3}_{-14.3}$	$51.1^{+8.8}_{-6.2}$	$31.9^{+11.6}_{-7.1}$	$24.2^{+8.4}_{-7.1}$	$15.2^{+6.2}_{-4.3}$	$11.6^{+5.1}_{-2.6}$
p_0 (Z)	0.01 (2.22)	0.03 (1.84)	0.24 (0.71)	0.20 (0.84)	0.50 (0.00)	0.24 (0.71)	0.50 (0.00)

Signal Region	RJR-G1a	RJR-G1b	RJR-G2a	RJR-G2b	RJR-G3a	RJR-G3b	RJR-G4
MC expected events							
Diboson	3.06	1.54	2.91	1.34	0.80	0.37	0.24
Z/γ^*+jets	28.56	13.03	28.01	9.41	8.56	2.90	2.05
W+jets	13.99	6.40	14.66	4.98	4.45	1.71	0.99
$t\bar{t}$(+EW) + single top	6.04	1.96	6.50	1.99	2.74	1.32	0.97
Fitted background events							
Diboson	3.1 ± 0.6	1.5 ± 0.4	2.9 ± 0.8	1.34 ± 0.34	0.8 ± 0.24	0.37 ± 0.22	0.24 ± 0.13
Z/γ^*+jets	23.9 ± 3.0	10.9 ± 1.5	23.6 ± 2.8	7.9 ± 1.1	7.22 ± 1.0	2.5 ± 0.6	1.73 ± 0.33
W+jets	11.4 ± 1.7	5.2 ± 0.8	11.7 ± 2.1	4.0 ± 0.7	3.5 ± 0.7	1.4 ± 0.6	0.79 ± 0.27
$t\bar{t}$(+EW) + single top	4.8 ± 2.1	1.6 ± 1.1	5.6 ± 2.8	1.7 ± 1.0	2.4 ± 1.1	$1.14^{+1.20}_{-1.14}$	$0.83^{+1.19}_{-0.83}$
Multi-jet	0.21 ± 0.21	–	0.6 ± 0.6	0.21 ± 0.21	–	–	–
Total bkg	43 ± 4	19.2 ± 2.2	44 ± 4	15.2 ± 1.7	13.9 ± 1.6	5.3 ± 1.4	3.6 ± 1.3
Observed	38	16	48	15	19	11	6
$\langle\epsilon\sigma\rangle^{95}_{\mathrm{obs}}$ [fb]	0.39	0.26	0.56	0.28	0.40	0.38	0.25
S^{95}_{obs}	13.9	9.4	20.1	10.0	14.5	13.6	9.1
S^{95}_{exp}	$16.2^{+6.6}_{-4.9}$	$10.7^{+4.1}_{-2.8}$	$17.4^{+5.4}_{-5.5}$	$9.5^{+4.2}_{-2.4}$	$9.7^{+4.0}_{-2.1}$	$10.2^{+3.8}_{-1.4}$	$7.6^{+2.3}_{-1.7}$
p_0 (Z)	0.50 (0.00)	0.50 (0.00)	0.23 (0.73)	0.50 (0.00)	0.09 (1.36)	0.12 (1.15)	0.18 (0.90)

Signal Region	RJR-C1	RJR-C2	RJR-C3	RJR-C4	RJR-C5
MC expected events					
Diboson	4.37	3.44	1.64	2.74	0.83
Z/γ^*+jets	24.41	20.58	7.23	10.18	2.32
W+jets	9.63	7.23	7.95	7.94	2.31
$t\bar{t}$(+EW) + single top	1.31	1.53	5.40	7.38	3.39
Fitted background events					
Diboson	4.37 ± 1.0	3.4 ± 0.8	1.6 ± 0.4	2.7 ± 0.6	0.8 ± 0.5
Z/γ^*+jets	21.6 ± 2.2	18.2 ± 1.9	6.0 ± 1.1	8.5 ± 1.2	2.1 ± 0.6
W+jets	9.3 ± 1.8	7.0 ± 1.3	8.3 ± 1.3	8.3 ± 1.4	2.7 ± 1.4
$t\bar{t}$(+EW) + single top	$0.93^{+1.06}_{-0.93}$	1.1 ± 0.7	3.3 ± 1.4	4.5 ± 2.6	$0.85^{+1.14}_{-0.85}$
Multi-jet	0.4 ± 0.4	–	0.6 ± 0.6	0.8 ± 0.8	0.4 ± 0.4
Total bkg	36.6 ± 3.4	29.7 ± 2.7	19.8 ± 2.4	24.8 ± 3.3	6.8 ± 1.4
Observed	31	25	12	21	8
$\langle\epsilon\sigma\rangle^{95}_{\mathrm{obs}}$ [fb]	0.34	0.29	0.22	0.30	0.24
S^{95}_{obs}	12.4	10.5	7.9	10.8	8.8
S^{95}_{exp}	$15.1^{+5.1}_{-5.2}$	$13.5^{+4.6}_{-4.0}$	$10.7^{+4.3}_{-2.5}$	$11.3^{+3.9}_{-1.2}$	$7.8^{+2.4}_{-1.9}$
p_0 (Z)	0.50 (0.00)	0.50 (0.00)	0.50 (0.00)	0.50 (0.00)	0.31 (0.51)

Table 6: Numbers of events observed in the signal regions used in the RJR-based analysis compared with background expectations obtained from the fits described in the text using pp collision data at $\sqrt{s} = 13$ TeV corresponding to an integrated luminosity of 36.1 fb^{-1}. Empty cells (indicated by a '-') correspond to estimates lower than 0.01. The p-values (p_0) give the probabilities of the observations being consistent with the estimated backgrounds. For an observed number of events lower than expected, the p-value is truncated at 0.5. Between parentheses, p-values are also given as the number of equivalent Gaussian standard deviations (Z). Also shown are 95% CL upper limits on the visible cross-section ($\langle\epsilon\sigma\rangle^{95}_{\mathrm{obs}}$), the visible number of signal events (S^{95}_{obs}) and the number of signal events (S^{95}_{exp}) given the expected number of background events (and $\pm 1\sigma$ excursions of the expectation).

Tables 5 and 6.

The model-dependent fits in all the SRs are then used to set limits on specific classes of SUSY models. The two searches presented in this document are combined such that the final combined observed and expected 95% CL exclusion limits are obtained from the signal regions with the best expected CL_s value.

In Figure 13, limits are shown for two classes of simplified models in which only direct production of light-flavour mass-degenerate squark or gluino pairs are considered. Limits are obtained by using the signal region with the best expected sensitivity at each point. In these simplified model scenarios, the upper limit of the excluded light-flavour squark mass region is 1.58 TeV assuming massless $\tilde{\chi}_1^0$, as obtained from the signal region RJR-S4. The corresponding limit on the gluino mass is 2.03 TeV, if the $\tilde{\chi}_1^0$ is massless, as obtained from the signal region Meff-4j-3000. The best sensitivity in the region of parameter space where the mass difference between the squark (gluino) and the lightest neutralino is small, is obtained from the dedicated RJR-C signal regions. In these regions with very compressed spectra and where mass difference < 50 GeV, squark (gluino) masses up to 650 GeV (1 TeV) are excluded.
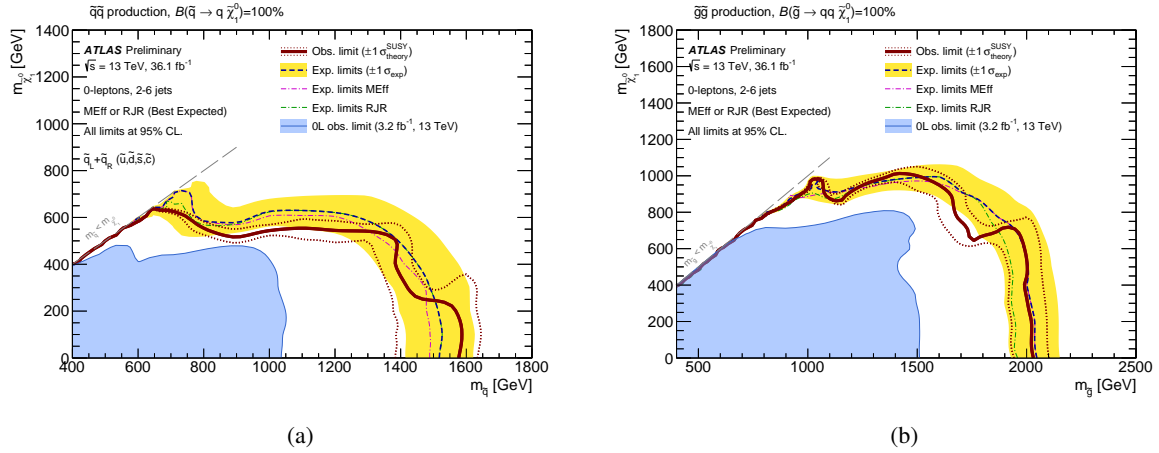
Figure 13: Exclusion limits for direct production of (a) light-flavour squark pairs with decoupled gluinos and (b) gluino pairs with decoupled squarks. Gluinos (light-flavour squarks) are required to decay to two quarks (one quark) and a neutralino LSP. Exclusion limits are obtained by using the signal region with the best expected sensitivity at each point. Expected limits from the Meff- and RJR-based searches separately are also shown for comparison. The blue dashed lines show the expected limits at 95% CL, with the light (yellow) bands indicating the 1σ excursions due to experimental and background-only theoretical uncertainties. Observed limits are indicated by medium dark (maroon) curves where the solid contour represents the nominal limit, and the dotted lines are obtained by varying the signal cross-section by the renormalization and factorization scale and PDF uncertainties. Results are compared with the observed limits obtained by the previous ATLAS searches with no leptons, jets and missing transverse momentum [11].

In Figure 14, limits are shown for pair-produced light-flavour squarks or gluinos each decaying via an intermediate $\tilde{\chi}_1^\pm$ to a quark (for squarks) or two quarks (for gluinos), a W boson and a $\tilde{\chi}_1^0$. Two sets of models of mass spectra are considered for each production. One is with a fixed $m_{\tilde{\chi}_1^\pm} = (m_{\tilde{g}} + m_{\tilde{\chi}_1^0})/2$ (or $(m_{\tilde{g}} + m_{\tilde{\chi}_1^0})/2$), the other is with a fixed $m_{\tilde{\chi}_1^0} = 60$ GeV. In the former models with squark-pair production, $m_{\tilde{q}}$ up to 1.15 TeV are excluded for a massless $\tilde{\chi}_1^0$, and $m_{\tilde{g}}$ up to 2.01 TeV with gluino-pair production. These limits are obtained from the signal region RJR-G2b and Meff-6j-2600, respectively. In the regions

with very compressed spectra with mass difference between gluino (or squark) and $\tilde{\chi}_1^0$ is less than 50 GeV, RJR-C signal regions also exclude squark (gluino) masses up to 600 GeV (1 TeV). In the latter models, Meff-2jB-1600 and Meff-2jB-2400 extend the limits on squark (gluino) masses up to 1.11 TeV (1.9 TeV) in the regions with small mass difference between squark (gluino) and $\tilde{\chi}_1^\pm$.

In Figure 15, limits are shown for gluino-pair production decaying via an intermediate $\tilde{\chi}_2^0$ to two quarks, a Z boson and a $\tilde{\chi}_1^0$. The mass of the $\tilde{\chi}_1^0$ is set to 1 GeV. In these models, gluino masses below 2.0 TeV are excluded for $\tilde{\chi}_2^0$ masses of $\sim$ 1 TeV, as obtained from the signal region Meff-6j-2600.

In Figure 16, results are presented in the models with mixed decays of intermediate $\tilde{\chi}_1^\pm$ and $\tilde{\chi}_2^0$ for squark-pair and gluino-pair production. The highest limits on squark mass are 1.34 TeV and on gluino mass are 2.02 TeV, which are similar to the models with 100% BR for $\tilde{\chi}_1^\pm$ or for $\tilde{\chi}_2^0$ to a Z boson and $\tilde{\chi}_1^0$.

In Figure 17, results are interpreted in models in simplified pMSSM models assuming only light-flavour squarks, gluino and $\tilde{\chi}_1^0$. The $\tilde{\chi}_1^0$ is assumed to be purely bino. Models with a fixed $m_{\tilde{\chi}_1^0} = 0, 695, 995$ GeV are considered varying $m_{\tilde{g}}$ and $m_{\tilde{q}}$. In the limit of high squark mass, the gluino mass up to 2 TeV are excluded for massless $\tilde{\chi}_1^0$ and it is consistent with the simplified models of gluino-pair prudction with decoupled limit of squarks. With a gluino mass at 6 TeV, squark masses up to 2.2 TeV are excluded for a massless $\tilde{\chi}_1^0$, much higher than the simplified models of squark-pair production with decoupled limit of gluino. This is due to large cross-section of $\tilde{q}\tilde{q}$ pair production via gluino exchange diagrams.

A comparison of the Meff-based and RJR-based results highlights some notable features. The RJR-Cx signal regions provide additional sensitivity in the most compressed mass regions beyond their Meff-based counterparts, extending exclusion limits up to 200 GeV in $\tilde{\chi}_1^0$ mass for the smallest mass-splitting, as is the case in Figure 14 (a) for light-flavour squarks decaying via an intermediate $\tilde{\chi}_1^\pm$. In general, the RJR-Cx regions are only mildy sensitive to the specific decays of squarks and gluinos, resulting in similar sensitivity as a function of $\tilde{q}/\tilde{g}$ and $\tilde{\chi}_1^0$ masses between signal models with direct decays in Figure 13 and those with intermediate sparticle decays as in Figure 14.

Despite being largely orthogonal, the RJR-based and Meff-based SRs targeting squark and gluino direct decay signals tend to result in similar sensitivity, with the RJR-based regions generally performing better for intermediate mass splittings. This is the result of tighter restrictions place on dimensionless variables in the RJR-based regions, resulting in generally lower background yields.

For models with additional jets in the final state expected from intermediate sparticle decays, the Meff-5j-x and Meff-6j-x provide significant additional sensitivity with respect to lower multiplicity SRs, extending exclusion limits close to 100 GeV in gluino mass when intermediate $\tilde{\chi}_1^\pm$ decays are considered. These more stringent jet multiplicity requirements compensate for the modest $E_T^{\text{miss}}/m_{\text{eff}}(N_j)$ values characteristic of these models.

With unique requirements aimed at tagging hadronic decays of W/Z bosons, the Meff-2jB-x SRs provide distinctive sensitivity to models with intermediate $\tilde{\chi}_1^\pm$ and $\tilde{\chi}_2^0$ decays when these sparticles are close to degenerate in mass with their parents squarks and gluinos, corresponding to Figures 14(b,d), 15, and 16. In these cases, the sensitivity of the Meff-2jB-x regions far surpasses those of the RJR-based and other Meff-based SRs.
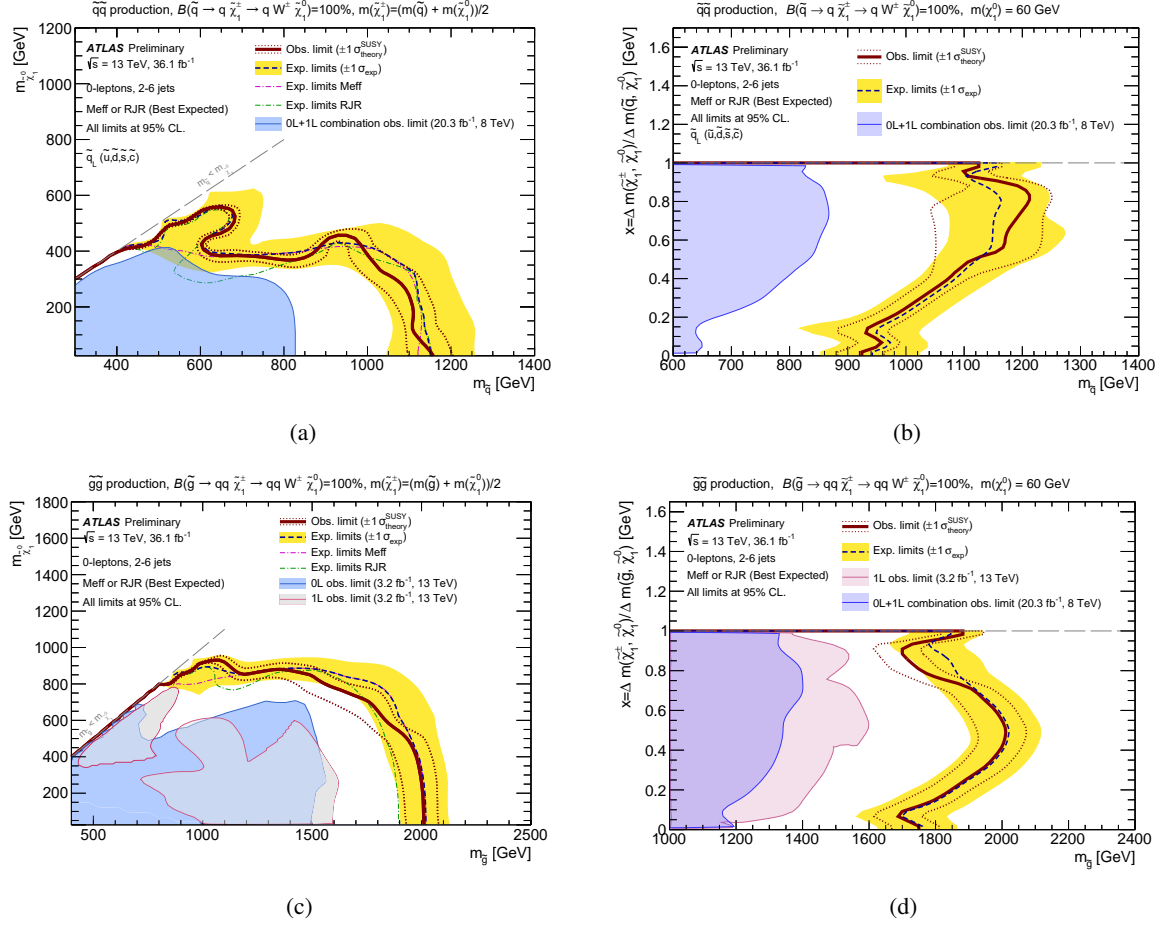
Figure 14: Exclusion limits for direct production of (a,b) light-flavour squark$_L$ pairs with decoupled gluinos and (c,d) gluino pairs with decoupled squarks. Gluinos (light-flavour squarks) are required to decay to two quarks (one quark) and an intermediate $\tilde{\chi}_1^\pm$, decaying to a W boson and a $\tilde{\chi}_1^0$. Models with (a,c) a fixed $m_{\tilde{\chi}_1^\pm} = (m_{\tilde{g}} + m_{\tilde{\chi}_1^0})/2$ (or $(m_{\tilde{q}} + m_{\tilde{\chi}_1^0})/2$) and varying values of $m_{\tilde{g}}$ (or $m_{\tilde{q}}$) and $m_{\tilde{\chi}_1^0}$, and (b,d) a fixed $m_{\tilde{\chi}_1^0} = 60$ GeV and varying values of $m_{\tilde{g}}$ (or $m_{\tilde{q}}$) and $m_{\tilde{\chi}_1^\pm}$ are considered. Exclusion limits are obtained by using the signal region with the best expected sensitivity at each point. Expected limits from the Meff- and RJR-based searches separately are also shown for comparison in (a,c). The blue dashed lines show the expected limits at 95% CL, with the light (yellow) bands indicating the 1σ excursions due to experimental and background-only theoretical uncertainties. Observed limits are indicated by medium dark (maroon) curves where the solid contour represents the nominal limit, and the dotted lines are obtained by varying the signal cross-section by the renormalization and factorization scale and PDF uncertainties. Results (a) are compared with the observed limits obtained by the previous ATLAS searches with no leptons or one lepton, jets and missing transverse momentum [18]. Results (c) are compared with the observed limits obtained by the previous ATLAS searches with no leptons or one lepton, jets and missing transverse momentum [11, 28]. Results (d) are compared with the observed limits obtained by the previous ATLAS searches with no leptons or one lepton, jets and missing transverse momentum [18, 28].
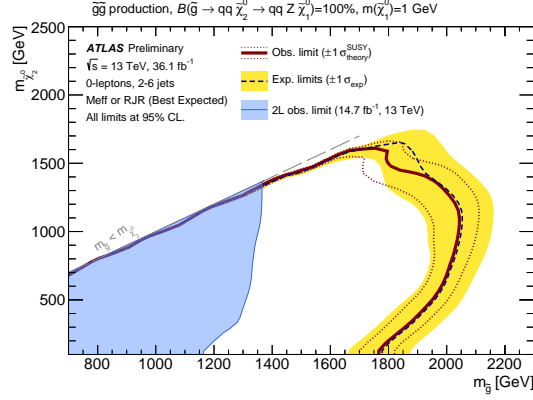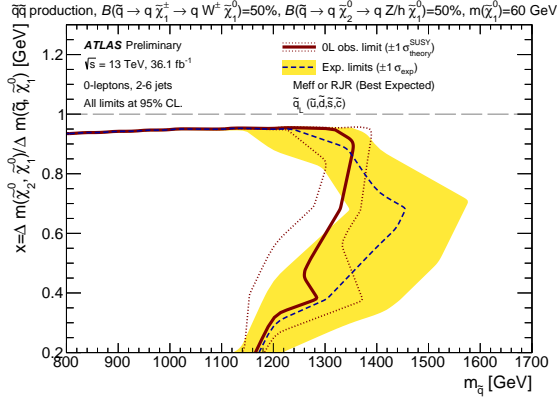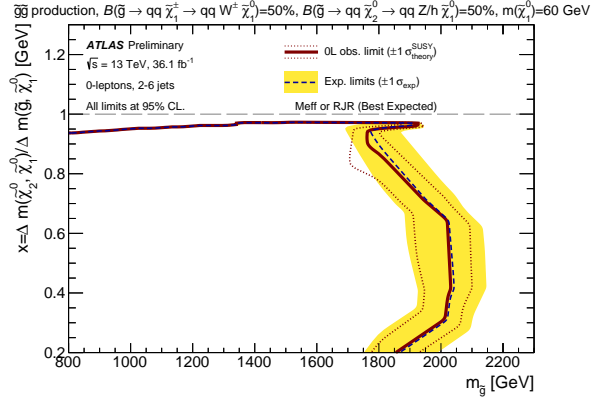
Figure 15: Exclusion limits for pair-produced gluinos each decaying via an intermediate $\tilde{\chi}_2^0$ to two quarks, a Z boson and a $\tilde{\chi}_1^0$ for models with a fixed $m_{\tilde{\chi}_1^0} = 1$ GeV and varying values of $m_{\tilde{g}}$ and $m_{\tilde{\chi}_2^0}$. Exclusion limits are obtained by using the signal region with the best expected sensitivity at each point. The blue dashed lines show the expected limits at 95% CL, with the light (yellow) bands indicating the 1σ excursions due to experimental and background-only theoretical uncertainties. Observed limits are indicated by medium dark (maroon) curves where the solid contour represents the nominal limit, and the dotted lines are obtained by varying the signal cross-section by the renormalization and factorization scale and PDF uncertainties. Results are compared with the observed limits obtained by the previous ATLAS search in events containing a leptonically decaying Z boson, jets and missing transverse momentum [103].

Figure 16: Exclusion limits for direct production of (a) light-flavour squark$_L$ pairs with decoupled gluinos and (b) gluino pairs with decoupled squarks. Gluinos (light-flavour squarks) are required to decay to two quarks (one quark) and a intermediate $\tilde{\chi}_1^\pm$ or $\tilde{\chi}_2^0$ at 50% BR, respectively. $\tilde{\chi}_1^\pm$ decays to a W boson and a $\tilde{\chi}_1^0$, and $\tilde{\chi}_2^0$ decays to a Z or a h boson and $\tilde{\chi}_1^0$. Models with a fixed $m_{\tilde{\chi}_1^0} = 60$ GeV are considered varying $m_{\tilde{g}}$ (or $m_{\tilde{q}}$) and $m_{\tilde{\chi}_1^0}$. Exclusion limits are obtained by using the signal region with the best expected sensitivity at each point. The blue dashed lines show the expected limits at 95% CL, with the light (yellow) bands indicating the 1σ excursions due to experimental and background-only theoretical uncertainties. Observed limits are indicated by medium dark (maroon) curves where the solid contour represents the nominal limit, and the dotted lines are obtained by varying the signal cross-section by the renormalization and factorization scale and PDF uncertainties.
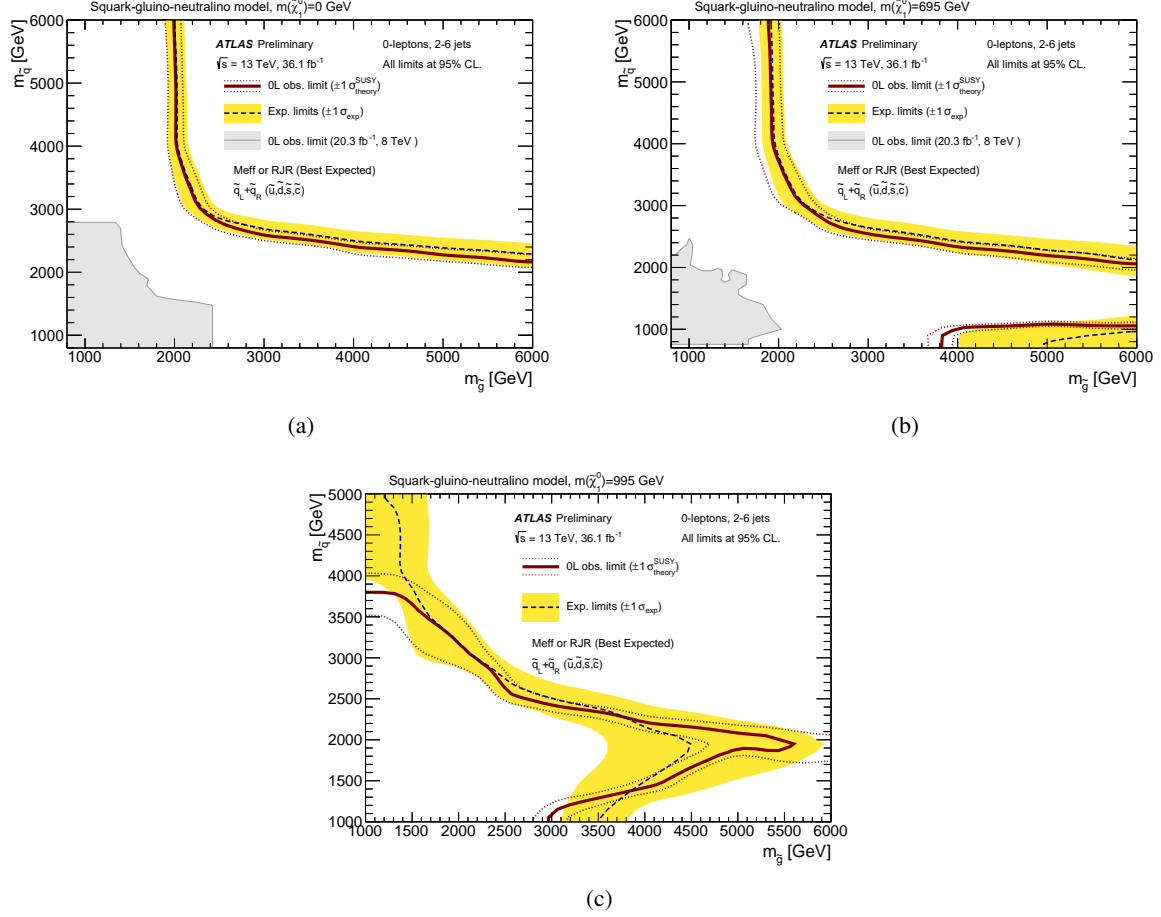
(a)

(b)

(c)

Figure 17: Exclusion limits for inclusive squark-gluino productions in pMSSM models with (a) $m_{\tilde{\chi}_1^0} = 0$ GeV, (b) $m_{\tilde{\chi}_1^0} = 695$ GeV and (c) $m_{\tilde{\chi}_1^0} = 995$ GeV varying values of $m_{\tilde{g}}$ and $m_{\tilde{q}}$ assuming purely bino $\tilde{\chi}_1^0$. Exclusion limits are obtained by using the signal region with the best expected sensitivity at each point. The blue dashed lines show the expected limits at 95% CL, with the light (yellow) bands indicating the 1σ excursions due to experimental and background-only theoretical uncertainties. Observed limits are indicated by medium dark (maroon) curves where the solid contour represents the nominal limit, and the dotted lines are obtained by varying the signal cross-section by the renormalization and factorization scale and PDF uncertainties. Results (a,b) are compared with the observed limits obtained by the previous ATLAS searches with no leptons, jets and missing transverse momentum [17].

11 Conclusion

This paper presents results of the two selection strategies to search for squarks and gluinos in final states containing high-p_T jets, large missing transverse momentum but no electrons or muons, based on a 36.1 fb^{-1} dataset of $\sqrt{s}$ = 13 TeV proton–proton collisions recorded by the ATLAS experiment at the LHC in 2015 and 2016.

Results are interpreted in terms of simplified models or pMSSM models with only light-flavour squarks, or gluinos, together with a neutralino LSP, with the masses of all the other SUSY particles decoupled. For a massless lightest neutralino, gluino masses below 2.03 TeV are excluded at the 95% confidence level in a simplified model with only gluinos and the lightest neutralino. For a simplified model involving the strong production of squarks of the first and second generations, with decays to a massless lightest neutralino, squark masses below 1.58 TeV are excluded, assuming mass-degenerate squarks of the first two generations. In simplified models with pair-produced squarks and gluinos, each decaying via an intermediate $\tilde{\chi}_1^{\pm}$ to one quark or two quarks, a W boson and a $\tilde{\chi}_1^0$, squark masses below 1.15 TeV and gluino masses below 2.01 TeV are excluded for massless $\tilde{\chi}_1^0$. In pMSSM models assuming squarks, gluinos and $\tilde{\chi}_1^0$, gluino masses below 2.0 TeV are excluded at squark mass at 6 TeV or squark masses below 2.2 TeV are excluded at gluino mass at 6 TeV for massless $\tilde{\chi}_1^0$.

These results substantially extend the region of supersymmetric parameter space excluded by previous LHC searches.

References

[1] Y. A. Golfand and E. P. Likhtman, *Extension of the Algebra of Poincare Group Generators and Violation of p Invariance*, JETP Lett. **13** (1971) 323, [Pisma Zh.Eksp.Teor.Fiz.13:452-455,1971].

[2] D. V. Volkov and V. P. Akulov, *Is the Neutrino a Goldstone Particle?*, Phys. Lett. B **46** (1973) 109.

[3] J. Wess and B. Zumino, *Supergauge Transformations in Four-Dimensions*, Nucl. Phys. B **70** (1974) 39.

[4] J. Wess and B. Zumino, *Supergauge Invariant Extension of Quantum Electrodynamics*, Nucl. Phys. B **78** (1974) 1.

[5] S. Ferrara and B. Zumino, *Supergauge Invariant Yang-Mills Theories*, Nucl. Phys. B **79** (1974) 413.

[6] A. Salam and J. A. Strathdee, *Supersymmetry and Nonabelian Gauges*, Phys. Lett. B **51** (1974) 353.

[7] G. R. Farrar and P. Fayet, *Phenomenology of the Production, Decay, and Detection of New Hadronic States Associated with Supersymmetry*, Phys. Lett. B **76** (1978) 575.

[8] L. Evans and P. Bryant, *LHC Machine*, JINST **3** (2008) S08001.

[9] P. Fayet, *Supersymmetry and Weak, Electromagnetic and Strong Interactions*, Phys. Lett. B **64** (1976) 159.

[10] P. Fayet, *Spontaneously Broken Supersymmetric Theories of Weak, Electromagnetic and Strong Interactions*, Phys. Lett. B **69** (1977) 489.

[11] ATLAS Collaboration, *Search for squarks and gluinos in final states with jets and missing transverse momentum at $\sqrt{s}$ = 13 TeV with the ATLAS detector*, Eur. Phys. J. C **76** (2016) 392, arXiv: 1605.03814 [hep-ex].

[12] M. R. Buckley et al., *Super-Razor and Searches for Sleptons and Charginos at the LHC*, Phys. Rev. **D89** (2014) 055020, arXiv: `1310.4827 [hep-ph]`.

[13] P. Jackson, C. Rogan and M. Santoni, *Sparticles in motion: Analyzing compressed SUSY scenarios with a new method of event reconstruction*, Phys. Rev. D **95** (2017) 035031, arXiv: `1607.08307 [hep-ex]`.

[14] ATLAS Collaboration, *Search for squarks and gluinos using final states with jets and missing transverse momentum with the ATLAS detector in $\sqrt{s}$ = 7 TeV proton-proton collisions*, Phys. Lett. B **701** (2011) 186, arXiv: `1102.5290 [hep-ex]`.

[15] ATLAS Collaboration, *Search for squarks and gluinos using final states with jets and missing transverse momentum with the ATLAS detector in $\sqrt{s}$ = 7 TeV proton-proton collisions*, Phys. Lett. B **710** (2012) 67, arXiv: `1109.6572 [hep-ex]`.

[16] ATLAS Collaboration, *Search for squarks and gluinos with the ATLAS detector in final states with jets and missing transverse momentum using 4.7 fb^{-1} of $\sqrt{s}$ = 7 TeV proton-proton collision data*, Phys. Rev. D **87** (2013) 012008, arXiv: `1208.0949 [hep-ex]`.

[17] ATLAS Collaboration, *Search for squarks and gluinos with the ATLAS detector in final states with jets and missing transverse momentum using $\sqrt{s}$ = 8 TeV proton–proton collision data*, JHEP **09** (2014) 176, arXiv: `1405.7875 [hep-ex]`.

[18] ATLAS Collaboration, *Summary of the searches for squarks and gluinos using $\sqrt{s}$ = 8 TeV pp collisions with the ATLAS experiment at the LHC*, JHEP **10** (2015) 054, arXiv: `1507.05525 [hep-ex]`.

[19] CMS Collaboration, *Search for supersymmetry in hadronic final states using MT2 in pp collisions at $\sqrt{s}$ = 7 TeV*, JHEP **10** (2012) 018, arXiv: `1207.1798 [hep-ex]`.

[20] CMS Collaboration, *Search for new physics in the multijet and missing transverse momentum final state in proton-proton collisions at $\sqrt{s}$ = 7 TeV*, Phys. Rev. Lett. **109** (2012) 171803, arXiv: `1207.1898 [hep-ex]`.

[21] CMS Collaboration, *Search for supersymmetry in hadronic final states with missing transverse energy using the variables α_T and b-quark multiplicity in pp collisions at 8 TeV*, Eur. Phys. J. C **73** (2013) 2568, arXiv: `1303.2985 [hep-ex]`.

[22] CMS Collaboration, *Inclusive search for supersymmetry using the razor variables in pp collisions at $\sqrt{s}$ = 7 TeV*, Phys. Rev. Lett. **111** (2013) 081802, arXiv: `1212.6961 [hep-ex]`.

[23] CMS Collaboration, *Search for new physics in the multijet and missing transverse momentum final state in proton-proton collisions at $\sqrt{s}$= 8 TeV*, JHEP **06** (2014) 055, arXiv: `1402.4770 [hep-ex]`.

[24] CMS Collaboration, *Searches for Supersymmetry using the M_{T2} Variable in Hadronic Events Produced in pp Collisions at 8 TeV*, JHEP **05** (2015) 078, arXiv: `1502.04358 [hep-ex]`.

[25] CMS Collaboration, *Search for new physics in final states with jets and missing transverse momentum in $\sqrt{s}$ = 13 TeV pp collisions with the α_T variable*, Submitted to EPJC (2016), arXiv: `1611.00338 [hep-ex]`.

[26] CMS Collaboration, *Inclusive search for supersymmetry using razor variables in pp collisions at $\sqrt{s}$ = 13 TeV*, Phys. Rev. D **95** (2017) 012003, arXiv: `1609.07658 [hep-ex]`.

[27] CMS Collaboration, *Search for new physics with the MT2 variable in all-jets final states produced in pp collisions at $\sqrt{s}$ = 13 TeV*, JHEP **10** (2016) 006, arXiv: `1603.04053 [hep-ex]`.

[28] ATLAS Collaboration, *Search for gluinos in events with an isolated lepton, jets and missing transverse momentum at $\sqrt{s}$ = 13 TeV with the ATLAS detector*, Eur. Phys. J. C **76** (2016), arXiv: 1605.04285 [hep-ex].

[29] J. Alwall et al., *Searching for Directly Decaying Gluinos at the Tevatron*, Phys. Lett. B **666** (2008) 34, arXiv: 0803.0019 [hep-ph].

[30] J. Alwall, P. Schuster and N. Toro, *Simplified Models for a First Characterization of New Physics at the LHC*, Phys. Rev. D **79** (2009) 075020, arXiv: 0810.3921 [hep-ph].

[31] D. Alves et al., *Simplified Models for LHC New Physics Searches*, J. Phys. G: Nucl. Part. Phys. **39** (2012) 105005, arXiv: 1105.2838 [hep-ph].

[32] A. Djouadi et al., *The Minimal supersymmetric standard model: Group summary report*, (1998), arXiv: hep-ph/9901246.

[33] C. F. Berger et al., *Supersymmetry Without Prejudice*, JHEP **02** (2009) 023, arXiv: 0812.0980 [hep-ph].

[34] ATLAS Collaboration, *The ATLAS Experiment at the CERN Large Hadron Collider*, JINST **3** (2008) S08003.

[35] ATLAS Collaboration, *ATLAS Insertable B-Layer Technical Design Report*, ATLAS-TDR-19 (2010), URL: http://cdsweb.cern.ch/record/1291633.

[36] ATLAS Collaboration, *Performance of the ATLAS Trigger System in 2015*, Submitted to EPJC (2016), arXiv: 1611.09661 [hep-ex].

[37] ATLAS Collaboration, *Improved luminosity determination in pp collisions at $\sqrt{s}$ = 7 TeV using the ATLAS detector at the LHC*, Eur. Phys. J. C **73** (2013) 2518, arXiv: 1302.4393 [hep-ex].

[38] J. Alwall, R. Frederix, S. Frixione, V. Hirschi, F. Maltoni, O. Mattelaer, H. -S. Shao, T. Stelzer, P. Torrielli, M. Zaro, *The automated computation of tree-level and next-to-leading order differential cross sections, and their matching to parton shower simulations*, JHEP **07** (2014) 079, arXiv: 1405.0301 [hep-ph].

[39] T. Sjöstrand et al., *An Introduction to PYTHIA 8.2*, Comput. Phys. Commun. **191** (2015) 159, arXiv: 1410.3012 [hep-ph].

[40] L. Lönnblad and S. Prestel, *Matching Tree-Level Matrix Elements with Interleaved Showers*, JHEP **03** (2012) 019, arXiv: 1109.4829 [hep-ph].

[41] ATLAS Collaboration, *Summary of ATLAS Pythia 8 tunes*, ATL-PHYS-PUB-2012-003 (2012), URL: http://cdsweb.cern.ch/record/1474107.

[42] R. D. Ball et al., *Parton distributions with LHC data*, Nucl. Phys. B **867** (2013) 244, arXiv: 1207.1303 [hep-ph].

[43] W. Beenakker et al., *Squark and gluino production at hadron colliders*, Nucl. Phys. B **492** (1997) 51, arXiv: hep-ph/9610490.

[44] A. Kulesza and L. Motyka, *Threshold resummation for squark-antisquark and gluino-pair production at the LHC*, Phys. Rev. Lett. **102** (2009) 111802, arXiv: 0807.2405 [hep-ph].

[45] A. Kulesza and L. Motyka, *Soft gluon resummation for the production of gluino-gluino and squark-antisquark pairs at the LHC*, Phys. Rev. D **80** (2009) 095004, arXiv: 0905.4749 [hep-ph].

[46] W. Beenakker et al., *Soft-gluon resummation for squark and gluino hadroproduction*, JHEP **12** (2009) 041, arXiv: 0909.4418 [hep-ph].

[47] W. Beenakker et al., *Squark and gluino hadroproduction*, Int. J. Mod. Phys. A **26** (2011) 2637, arXiv: 1105.1110 [hep-ph].

[48] C. Borschensky et al., *Squark and gluino production cross sections in pp collisions at $\sqrt{s}$ = 13, 14, 33 and 100 TeV*, Eur. Phys. J. C **74** (2014) 3174, arXiv: 1407.5066 [hep-ph].

[49] ATLAS Collaboration, *Monte Carlo Generators for the Production of a W or Z/γ^* Boson in Association with Jets at ATLAS in Run 2*, ATL-PHYS-PUB-2016-003 (2016), URL: http://cds.cern.ch/record/2120133.

[50] T. Gleisberg et al., *Event generation with SHERPA 1.1*, JHEP **02** (2009) 007, arXiv: 0811.4622 [hep-ph].

[51] T. Gleisberg and S. Höche, *Comix, a new matrix element generator*, JHEP **12** (2008) 039, arXiv: 0808.3674 [hep-ph].

[52] F. Cascioli, P. Maierhofer and S. Pozzorini, *Scattering Amplitudes with Open Loops*, Phys. Rev. Lett. **108** (2012) 111601, arXiv: 1111.5206 [hep-ph].

[53] S. Schumann and F. Krauss, *A Parton shower algorithm based on Catani-Seymour dipole factorisation*, JHEP **03** (2008) 038, arXiv: 0709.1027 [hep-ph].

[54] S. Höche et al., *QCD matrix elements + parton showers: The NLO case*, JHEP **04** (2013) 027, arXiv: 1207.5030 [hep-ph].

[55] S. Höche, F. Krauss, S. Schumann and F. Siegert, *QCD matrix elements and truncated showers*, JHEP **05** (2009) 053, arXiv: 0903.1219 [hep-ph].

[56] R. D. Ball et al., *Parton distributions for the LHC Run II*, JHEP **04** (2015) 040, arXiv: 1410.8849 [hep-ph].

[57] H.-L. Lai et al., *New parton distributions for collider physics*, Phys. Rev. D **82** (2010) 074024, arXiv: 1007.2241 [hep-ph].

[58] F. P. R. Gavin Y. Li and S. Quackenbush, *FEWZ 2.0: A code for hadronic Z production at next-to-next-to-leading order*, Comput. Phys. Commun. **182** (2011) 2388, arXiv: 1011.3540 [hep-ph].

[59] ATLAS Collaboration, *Simulation of top quark production for the ATLAS experiment at $\sqrt{s}$ = 13 TeV*, ATL-PHYS-PUB-2016-004 (2016), URL: http://cds.cern.ch/record/2120417.

[60] S. Alioli et al., *A general framework for implementing NLO calculations in shower Monte Carlo programs: the POWHEG BOX*, JHEP **06** (2010) 043, arXiv: 1002.2581 [hep-ph].

[61] P. Artoisenet et al., *Automatic spin-entangled decays of heavy resonances in Monte Carlo simulations*, JHEP **03** (2013) 015, arXiv: 1212.3460 [hep-ph].

[62] T. Sjöstrand, S. Mrenna and P. Skands, *PYTHIA 6.4 Physics and Manual*, JHEP **05** (2006) 026, arXiv: hep-ph/0603175.

[63] J. Pumplin et al., *New generation of parton distributions with uncertainties from global QCD analysis*, JHEP **07** (2002) 012, arXiv: hep-ph/0201195.

[64] P. Z. Skands, *Tuning Monte Carlo Generators: The Perugia Tunes*, Phys. Rev. D **82** (2010) 074018, arXiv: 1005.3457 [hep-ph].

[65] M. Czakon, P. Fiedler and A. Mitov, *Total Top-Quark Pair-Production Cross Section at Hadron Colliders Through $O(\alpha_S^4)$*, Phys. Rev. Lett. **110** (2013) 252004, arXiv: 1303.6254 [hep-ph].

[66] M. Czakon and A. Mitov, *Top++: A Program for the Calculation of the Top-Pair Cross-Section at Hadron Colliders*, Comput. Phys. Commun. **185** (2014) 2930, arXiv: 1112.5675 [hep-ph].

[67] M. Aliev et al., *HATHOR: HAdronic Top and Heavy quarks crOss section calculatoR*, Comput. Phys. Commun. **182** (2011) 1034, arXiv: `1007.1327 [hep-ph]`.

[68] P. Kant et al., *HatHor for single top-quark production: Updated predictions and uncertainty estimates for single top-quark production in hadronic collisions*, Comput. Phys. Commun. **191** (2015) 74, arXiv: `1406.4403 [hep-ph]`.

[69] N. Kidonakis, *Two-loop soft anomalous dimensions for single top quark associated production with a W- or H-*, Phys. Rev. D **82** (2010) 054018, arXiv: `1005.4451 [hep-ph]`.

[70] N. Kidonakis, *Next-to-next-to-leading-order collinear and soft gluon corrections for t-channel single top quark production*, Phys. Rev. D **83** (2011) 091503, arXiv: `1103.2792 [hep-ph]`.

[71] ATLAS Collaboration, *Modelling of the $t\bar{t}H$ and $t\bar{t}V$ ($V = W, Z$) processes for $\sqrt{s}$ = 13 TeV ATLAS analyses*, ATL-PHYS-PUB-2016-005 (2016), URL: `http://cds.cern.ch/record/2120826`.

[72] K. M. A. Lazopoulos T. McElmurry and F. Petriello, *Next-to-leading order QCD corrections to $t\bar{t}Z$ production at the LHC*, Phys. Lett. B **666** (2008) 62, arXiv: `0804.2220 [hep-ph]`.

[73] J. M. Campbell and R. K. Ellis, *$t\bar{t}W^{\pm}$ production and decay at NLO*, JHEP **07** (2012) 052, arXiv: `1204.5678 [hep-ph]`.

[74] ATLAS Collaboration, *Multi-Boson Simulation for 13 TeV ATLAS Analyses*, ATL-PHYS-PUB-2016-002 (2016), URL: `http://cds.cern.ch/record/2119986`.

[75] ATLAS Collaboration, *The ATLAS Simulation Infrastructure*, Eur. Phys. J. C **70** (2010) 823, arXiv: `1005.4568 [physics.ins-det]`.

[76] S. Agostinelli et al., *GEANT4: A simulation toolkit*, Nucl. Instrum. Meth. A **506** (2003) 250.

[77] ATLAS Collaboration, *The simulation principle and performance of the ATLAS fast calorimeter simulation FastCaloSim*, ATL-PHYS-PUB-2010-013 (2010), URL: `http://cds.cern.ch/record/1300517`.

[78] D. J. Lange, *The EvtGen particle decay simulation package*, Nucl. Instrum. Meth. A **462** (2001) 152.

[79] A. D. Martin, W. J. Stirling, R. S. Thorne, G. Watt, *Parton distributions for the LHC*, Eur. Phys. J. C **63** (2009) 189, arXiv: `0901.0002 [hep-ph]`.

[80] M. Cacciari, G. P. Salam and G. Soyez, *The anti-k_t jet clustering algorithm*, JHEP **04** (2008) 063, arXiv: `0802.1189 [hep-ph]`.

[81] M. Cacciari and G. P. Salam, *Dispelling the N^3 myth for the k_t jet-finder*, Phys. Lett. B **641** (2006) 57, arXiv: `hep-ph/0512210`.

[82] ATLAS Collaboration, *Topological cell clustering in the ATLAS calorimeters and its performance in LHC Run 1*, Submitted to EPJC (2016), arXiv: `1603.02934 [hep-ex]`.

[83] M. Cacciari and G. P. Salam, *Pileup subtraction using jet areas*, Phys. Lett. B **659** (2008) 119, arXiv: `0707.1378 [hep-ph]`.

[84] ATLAS Collaboration, *Performance of pile-up mitigation techniques for jets in pp collisions at $\sqrt{s}$ = 8 TeV using the ATLAS detector*, Eur. Phys. J. C **76** (2016) 581, arXiv: `1510.03823 [hep-ex]`.

[85] ATLAS Collaboration, *Jet Calibration and Systematic Uncertainties for Jets Reconstructed in the ATLAS Detector at $\sqrt{s}$ = 13 TeV*, ATL-PHYS-PUB-2015-015 (2015), URL: `http://cdsweb.cern.ch/record/2037613`.

[86] ATLAS Collaboration, *Performance of b-Jet Identification in the ATLAS Experiment*, JINST **11** (2016) P04008, arXiv: 1512.01094 [hep-ex].

[87] ATLAS Collaboration, *Optimisation of the ATLAS b-tagging performance for the 2016 LHC Run*, ATL-PHYS-PUB-2016-012 (2016), URL: http://cds.cern.ch/record/2160731.

[88] ATLAS Collaboration, *Selection of jets produced in proton-proton collisions with the ATLAS detector using 2015 data*, ATLAS-CONF-2015-029 (2015), URL: http://cdsweb.cern.ch/record/2037702.

[89] ATLAS Collaboration, *Tagging and suppression of pileup jets with the ATLAS detector*, ATLAS-CONF-2014-018 (2014), URL: http://cds.cern.ch/record/1700870.

[90] ATLAS Collaboration, *Muon reconstruction performance of the ATLAS detector in proton–proton collision data at $\sqrt{s}$ =13 TeV*, Eur. Phys. J. C **76** (2016) 292, arXiv: 1603.05598 [hep-ex].

[91] ATLAS Collaboration, *Electron efficiency measurements with the ATLAS detector using the 2015 LHC proton-proton collision data*, ATLAS-CONF-2016-024 (2016), URL: http://cds.cern.ch/record/2157687.

[92] ATLAS Collaboration, *Expected performance of missing transverse momentum reconstruction for the ATLAS detector at $\sqrt{s}$ = 13 TeV*, ATL-PHYS-PUB-2015-023 (2015), URL: http://cdsweb.cern.ch/record/2037700.

[93] ATLAS Collaboration, *Measurement of the photon identification efficiencies with the ATLAS detector using LHC Run-1 data*, Eur. Phys. J. C **76** (2016) 666, arXiv: 1606.01813 [hep-ex].

[94] B. Nachman, P. Nef, A. Schwartzman, M. Swiatlowski, C. Wanotayaroj, *Jets from Jets: Reclustering as a tool for large radius jet reconstruction and grooming at the LHC*, JHEP **02** (2015) 075, arXiv: 1407.2922 [hep-ph].

[95] M. Baak et al., *HistFitter software framework for statistical data analysis*, Eur. Phys. J. C **75** (2015) 153, arXiv: 1410.1280 [hep-ex].

[96] A. L. Read, *Presentation of Search Results: The CL(s) Technique*, J. Phys. G **28** (2002) 2693.

[97] I. Hinchliffe et al., *Precision SUSY measurements at CERN LHC*, Phys. Rev. **D55** (1997) 5520, arXiv: hep-ph/9610544.

[98] C. Chen, *New approach to identifying boosted hadronically decaying particles using jet substructure in its center-of-mass frame*, Phys. Rev. D **85** (2012) 034007, arXiv: 1112.2567 [hep-ph].

[99] ATLAS Collaboration, *Jet energy measurement with the ATLAS detector in proton-proton collisions at $\sqrt{s}$ = 7 TeV*, Eur. Phys. J. C **73** (2013) 2304, arXiv: 1112.6426 [hep-ex].

[100] ATLAS Collaboration, *Single hadron response measurement and calorimeter jet energy scale uncertainty with the ATLAS detector at the LHC*, Eur. Phys. J. C **73** (2013) 2305, arXiv: 1203.1302 [hep-ex].

[101] ATLAS Collaboration, *Jet energy resolution in proton-proton collisions at $\sqrt{s}$ = 7 TeV recorded in 2010 with the ATLAS detector*, Eur. Phys. J. C **73** (2013) 2306, arXiv: 1210.6210 [hep-ex].

[102] ATLAS Collaboration, *Jet mass reconstruction with the ATLAS Detector in early Run 2 data*, ATLAS-CONF-2016-035 (2016), URL: http://cds.cern.ch/record/2200211.

[103] ATLAS Collaboration, *Search for new phenomena in events containing a same-flavour opposite-sign dilepton pair, jets, and large missing transverse momentum in $\sqrt{s}$ = 13 TeV pp collisions with the ATLAS detector*, Submitted to EPJC (2016), arXiv: 1611.05791 [hep-ex].